REPORT DOCUMENTATION PAGE

Form Approved
OMB No. 0704-0188

1. REPORT DATE *(DD-MM-YYYY)*	**2. REPORT TYPE**	**3. DATES COVERED** *(From - To)*
09/19/2022	Technical Report	Dec, 2020 - May, 2022

4. TITLE AND SUBTITLE

Characterization of 316 Stainless Steel and Inconel C-276 Degradation after Exposure up to 10 vol% H2S at High-Temperatures up to 100 Hours

5a. CONTRACT NUMBER

5b. GRANT NUMBER

5c. PROGRAM ELEMENT NUMBER

6. AUTHOR(S)

Theodore E. Burye
Talia M. Sebastian

5d. PROJECT NUMBER

5e. TASK NUMBER

5f. WORK UNIT NUMBER

7. PERFORMING ORGANIZATION NAME(S) AND ADDRESS(ES)

US Army CCDC Ground Vehicle Systems Center (GVSC)
Ground Vehicle Power and Mobility (GVPM)
Force Projection Technology (FPT)
6501 E. 11 Mile Road
Warren, MI 48397

8. PERFORMING ORGANIZATION REPORT NUMBER

OPSEC 6882

9. SPONSORING / MONITORING AGENCY NAME(S) AND ADDRESS(ES)

US Army CCDC Ground Vehicle Systems Center (GVSC)
Ground Vehicle Power and Mobility (GVPM)
Force Projection Technology (FPT)
6501 E. 11 Mile Road
Warren, MI 48397

10. SPONSOR/MONITOR'S ACRONYM(S)

11. SPONSOR/MONITOR'S REPORT NUMBER(S)

12. DISTRIBUTION / AVAILABILITY STATEMENT

DISTRIBUTION A. Approved for public release; distribution unlimited. OPSEC #6882

13. SUPPLEMENTARY NOTES

14. ABSTRACT

The purpose of this effort was to the study the potential compositional and structural changes in the materials used in the reactor used for the La0.7Sr0.3VO3.86-delta (LSV) sulfur tolerance In-house Laboratory Independent Research (ILIR) project. This effort was deemed appropriate and necessary after it was observed that after approximately 1.5 years of operation, using hydrogen sulfide (H2S) concentrations as high as 10 vol% and temperatures up to 700°C, the reactor lid formed a leak producing a small flame, which was a safety hazard. This study investigated if other locations within the reactor were potentially compromised, which could have caused additional safety issues. Additionally, due to the extreme operating conditions, this study took note of any other material changes in the reactor, which would decrease application confidence in using these materials again in future projects.

15. SUBJECT TERMS

16. SECURITY CLASSIFICATION OF: Available for Public Release			**17. LIMITATION OF ABSTRACT**	**18. NUMBER OF PAGES**	**19a. NAME OF RESPONSIBLE PERSON**
a. REPORT	**b. ABSTRACT**	**c. THIS PAGE**	Same as Report (SAR)	46	Theodore Burye
UNCLS	UNCLAS	UNCLAS			**19b. TELEPHONE NUMBER** *(include area code)* 586-282-3047

Characterization of 316 Stainless Steel and Inconel C-276 Degradation after Exposure up to 10 vol% H_2S at High-Temperatures up to 100 Hours

Theodore Burye[a] & Talia Sebastian[b]
U.S. Army Combat Capabilities Development Command Ground Vehicle Systems Center
Ground Vehicle Power & Mobility[a], Force Projection Technology[b]

Prepared by:

Dr. Theodore Burye
Chemical Engineer
theodore.e.burye2.civ@army.mil
Fuel Cell Technologies
Ground Vehicle Power and Mobility (GVPM)
Combat Capabilities Development Command (CCDC) Ground Vehicle Systems Center (GVSC)

Dr. Talia Sebastian
Research Chemist
talia.m.sebastian.civ@army.mil
Fuels and Lubricants Branch
Force Protection Technology (FPT)
Combat Capabilities Development Command (CCDC) Ground Vehicle Systems Center (GVSC)

Acknowledgements

X-ray Diffraction (XRD) data was acquired from the Ground Vehicle Systems Centers (GVSC's) Metallurgy laboratory. Demetrios Tzelepis and Ian Toppler, from the Characterization & Failure Analysis group, assisted with operation of the XRD equipment.

Table of Contents

List of Figures

List of Tables

1.0 Introduction

The purpose of this effort was to the study the potential compositional and structural changes in the materials used in the reactor used for the $La_{0.7}Sr_{0.3}VO_{3.86-\delta}$ (LSV) sulfur tolerance In-house Laboratory Independent Research (ILIR) project. This effort was deemed appropriate and necessary after it was observed that after approximately 1.5 years of operation, using hydrogen sulfide (H_2S) concentrations as high as 10vol% and temperatures up to 700°C, the reactor lid formed a leak producing a small flame, which was a safety hazard. This study investigated if other locations within the reactor were potentially compromised, which could have caused additional safety issues. Additionally, due to the extreme operating conditions, this study took note of any other material changes in the reactor, which would decrease application confidence in using these materials again in future projects.

2.0 Experimental Methods

2.1 LSV Experimental Setup, Testing Parameters and Untested Material Inspection

Between 2-2.5g of loose neat LSV powder (Praxair Surface Technologies; Woodinville, WA, USA) was placed inside a 99.5% high-purity alumina crucible (LSP Industrial Ceramics, Myrtle Beach, SC, USA), inside a sealed metal sample chamber (i.e., reactor), which was also insulated using high-temperature cloth insulation. This reactor was used to heat the material in different atmospheric compositions containing H_2S gas, shown in Figure 1. The use of H_2S simulates sulfur exposure from the fuel fed to fuel cell anodes directly or from reformer reformate. Due to H_2S gas being corrosive to metals, especially at elevated temperatures, the sample chamber and bolts used to seal the sample chamber were constructed from Inconel C-276, which has a high corrosion resistance. A seal was also placed between the lid and body, constructed of vermiculite, which has a high meting temperature and prevents H_2S gas from leaving. All other components, including an inlet extension tube place down inside the alumina crucible to direct gas flow, were constructed using 316 stainless steel (SS). The sample chamber was heated using heat tape with a maximum operating temperature of 760°C (Model BW0101020L) from BriskHeat (BriskHeat, Columbus, OH, USA). Nitrogen gas was used during the heating and cooling process, to prevent LSV samples from oxidizing.

Once each sample reached its steady state temperature, an H_2S-containing mixture (30ppm, 300ppm and 10 vol%), balanced with hydrogen (H_2) or methane (CH_4) gas, was introduced, simulating anode exposure to hydrogen or light hydrocarbon fuels. Samples were exposed to the gas while simultaneously being heated between 400-700°C for up to 100 hours. The sample chamber was returned to room temperature every 25 hours and sub-samples of loose LSV powder were removed for characterization of sulfur content and material property changes.

Prior to the system construction, shown in Figure 1, the reactor body and lid were machined from Inconel C-276 bar-round. The fittings and tubes, which were 316 SS, were purchased and installed pre-made. The following optical microscopy images, Figure 2 through Figure 5, illustrate the phases of the reactor body and lid construction, which were machined separately and then assembled. These images also provide a good visual comparison of how the different materials looked prior to experimentation.

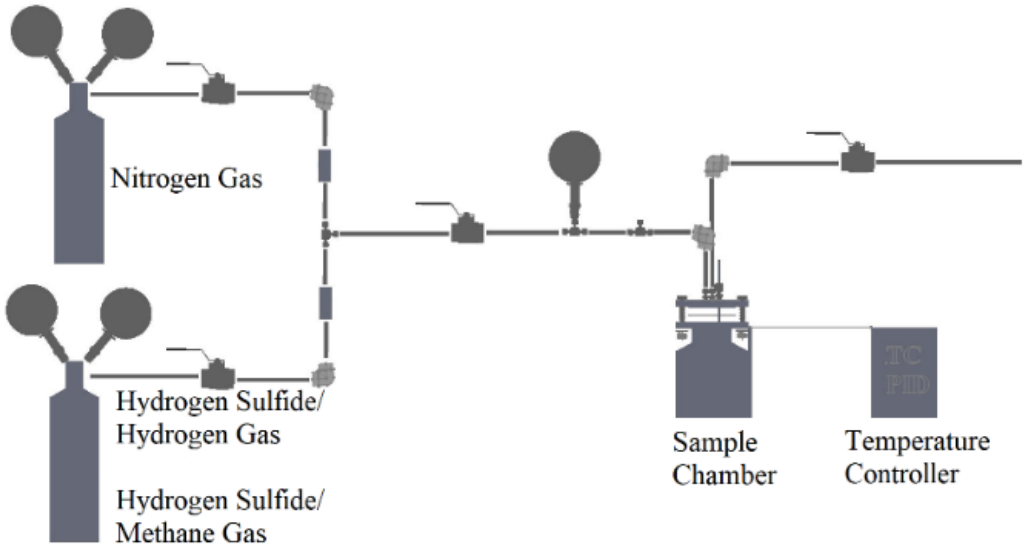

Figure 1: Experimental equipment setup used to expose LSV and Ni-YSZ loose powder to different sulfur concentration containing atmospheres between 400-700°C up to 100 hours.

Figure 2 and Figure 3 show optical microscopy pictures of the reactor body and lid, respectively, before experimental testing occurred. As mentioned above, the reactor body and lid were constructed using Inconel C-276, which is a high-corrosion resistant material.

Figure 4 details how the reactor body, lid and other necessary fittings, inlet tubes, exit tubes were connected. The tubes and fittings entering and exiting the lid were constructed of 316 SS, which is not as corrosion resistant as Inconel C-286. The inlet extension tube and fitting on the underside of the lid, not visible here, were also constructed from 316 SS.

Figure 2: Machined Untested Reactor Body

Figure 3: Machined Untested Reactor Lid

Figure 4: Machined Untested Assembled Reactor Body, Lid, Fittings and Tubing

Figure 5 details the final assembly of Figure 4, wrapped with high-temperature insulation, connected to the piping components directing gas to the reactor.

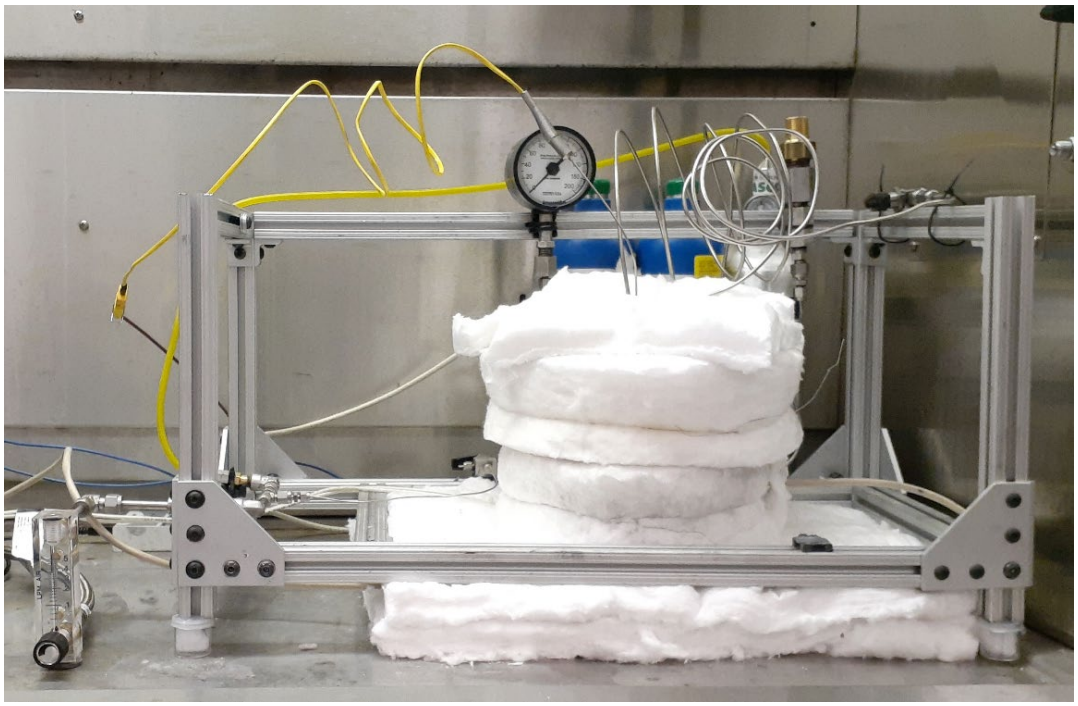

Figure 5: LSV Powder Test System Equipment with Gas Piping Components

2.2 Post-Mortem Material Analysis Methods

After over 1,200 hours of experimentation exposing the different components to H_2S gas, with concentrations as high as 10 vol% and temperatures as elevated as 700°C, the reactor assembly (Figure 4) was disassembled for characterization, with the following objectives: first to characterize the 316 SS and Inconel C-276 exposure to prolonged periods of elevated H_2S concentration, of which knowledge is currently limited and therefore a better understanding of material degradation is needed, and secondly this analysis provides a basis on how reliable these materials are for future projects and whether these materials are adequate choices in the roles they were used in.

To gain a better understanding of the elemental and material changes that occurred to each material in their different placements, the parts were sectioned using a cutting saw, in addition to conducting an analysis of the material surface. Figure 6 through Figure 8, show the material components that were analyzed, and the sectioning cuts used for characterization. Additionally, the insulation and the heat tape were analyzed.

Figure 6 shows details the locations of the 316 SS material that was analyzed. There were two pieces, with one being the inlet tube fitting located on the top of the lid and the second being the inlet tube extension located underneath the lid. The inlet tube fitting had its interior metal and gas through hole analyzed (#1) by sectioning the part using a cutting blade. The surface of the inlet tube fitting was also analyzed (#2). The inlet tube extension has its interior metal, gas through hole, and surface analyzed in the same manner (#3-4).

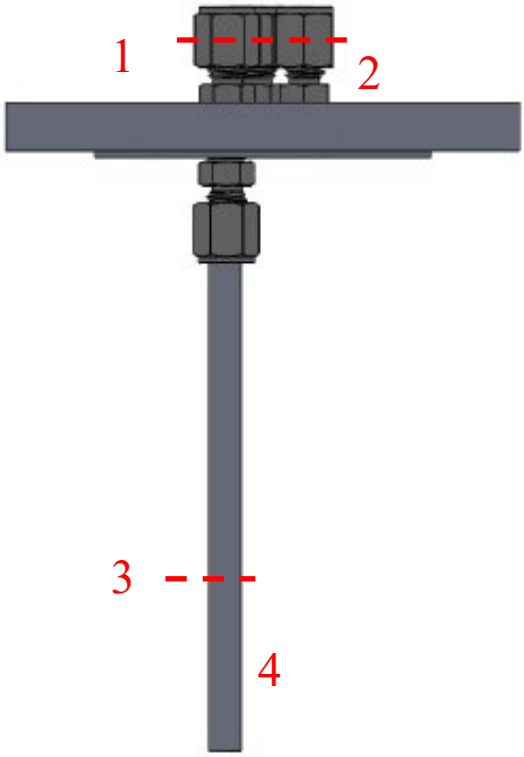

Figure 6: 316 SS Material Analysis Locations

Figure 7 details the top (left) and side (right) views of the reactor lid and the locations where it was analyzed. There were seven locations analyzed in total, which helped to map out variations in contamination concentrations with respect to lid material thickness and radii from the reactor lid center. Points #5, #6 and #7 analyzed contamination depth concentrations at the center of the lid going from the top (#5, exposed to air) of the lid to the underside (#7, exposed to inlet gasses). Points #8, #9 and #10 analyzed contamination depth concentrations halfway between the outer edge of the lid and the center going from the top (#8) to the underside (#10). Finally, point #11 looked at contamination concentrations at the outer surface of the lid at the outer radii of the lid.

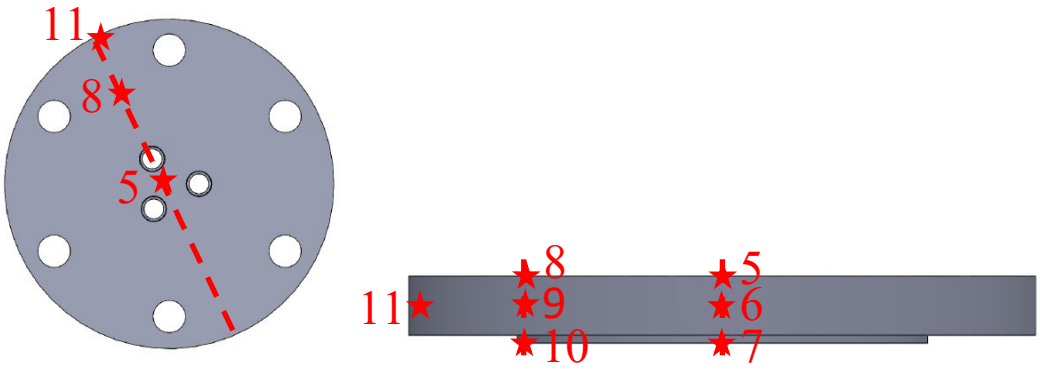

Figure 7: Inconel C-276 Reactor Lid Analysis Locations

Figure 8 details the side opaque (left) and side wireframe (right) views of the reactor body and the locations where it was analyzed. There were only three locations on the body, compared to seven for the lid. There are less analysis locations here because the top of the body is assumed to be similar to the lid in composition and operating temperature, and the neck section (immediately underneath the top) is similar to the analysis points listed as it would have a similar temperature profile and would be exposed to similar levels of contaminants, and the bottom sections of the reactor were not analyzed since the LSV powder and H_2S gas were never in contact with the bottom (i.e, the inlet tube never reached that far and gases rise). Finally, the body is a cylinder so any findings would be expected to be symmetrical as contaminant exposure was across the entire interior shaft surface and the reactor body was heater around its entire circumference. These three analysis points are measuring elemental and structural changes around where the inlet tube ended and where the heat tape was located to obtain the maximum contaminant and operating temperature exposure.

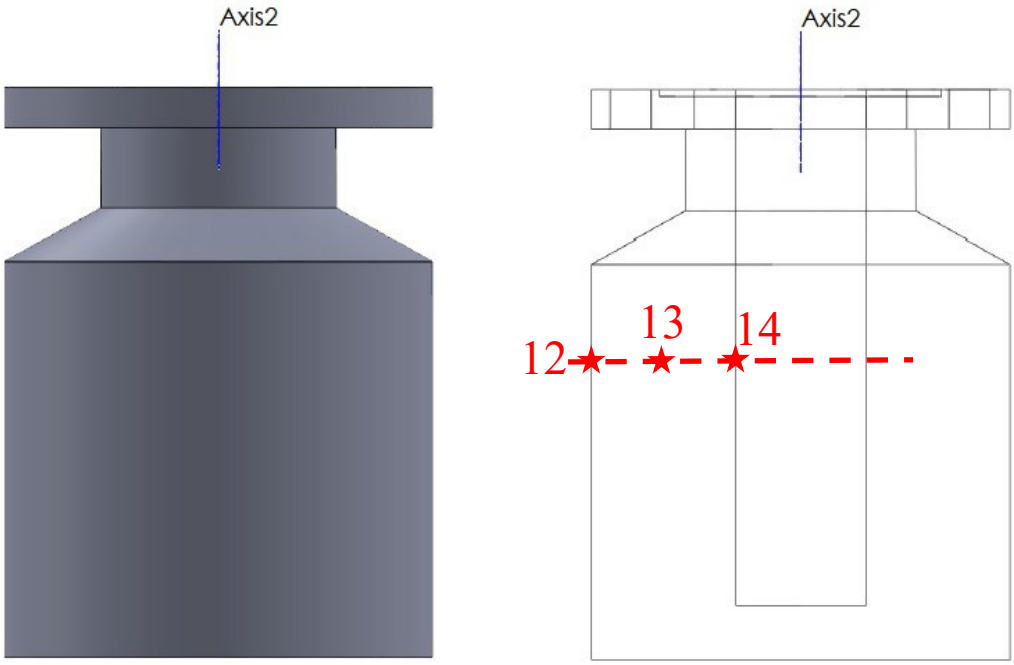

Figure 8: Inconel C-276 Reactor Body Analysis Locations

2.3 Characterization Methods

2.3.1 Scanning Electron Microscopy (SEM) and Energy Dispersive Spectroscopy (EDS) Experiments

Sulfur peak intensities were measured before and after each experiment using a Hitachi SEM (Hitachi; Krefeld, Germany) with an Oxford Instruments EDS detector (Oxford Instruments; Concord, MA, USA). EDS measurements were taken using a beam voltage of 20.0 kV, a 30 µm aperture, a 512 s scan speed, a 10 mm working distance, and a 100x magnification. At least four measurements were taken and averaged for each sub-sample to account for variations.

2.3.2 X-Ray Diffraction (XRD) Experiments

XRD was used to characterize changes to the crystal structure of each sub-sample every 25 hours after being exposed to the different H_2S concentrations and operating temperatures. A SmartLab XRD (Rigaku Americas Corporation; The Woodlands, TX, USA) was operated at 40 kV and 44 mA at room temperature. Scans were taken between $10° \leq 2\theta \leq 90°$ Two-Theta using a 0.020 step, 2.00s scan speed, copper filament and nickel filter. The diffraction peaks were identified from the Inorganic Crystal Structure Database (ICSD).

3.0 Results

The following analysis examined the changes in the elemental composition and structure of the 316 SS and Inconel C-276 materials at the analysis points previously mentioned, for the purpose 316 SS of examining material corrosion, which may occur due to the corrosive nature of H_2S and the high-temperatures used. Cracks formed from corrosion were the primary failure mode of concern, which could lead to the loss of reactant gas before exposure to the LSV powder samples, which would compromise results. Additionally, leaks could also pose a safety concern and should be mitigated if possible. Analysis of other failure modes, such as mechanical stress fractures, were not viewed as likely, and thus were not analyzed for since the equipment was not subjected to mechanical stress or any substantial loads. Additional testing of different failure modes may be conducted in the future if required.

EDS is typically, as a rule, unreliable at accurately measuring carbon and oxygen elemental compositions. The raw EDS results will show carbon and oxygen, but their wt% values are not listed here since they are unreliable. Any large-scale magnitude raw data changes in these elements may be discussed, such as if oxidation, if applicable.

3.1 316 Stainless Steel Characterization Results

The 316 SS material was analyzed first due to it lower corrosion resistance, compared to Inconel C-276, to determine if it was significantly compromised.

3.1.1 316 SS Fitting Results

Figure 9 details the SEM micrograph on the surface for the pristine 316 SS sample. The surface has a few micro-cracks, but otherwise is clean and has no large pitting or gouges on the surface, which influence results.

Figure 10 details the raw EDS results from an untested 316 SS fitting. This is a baseline to see if significant elemental changes occurred in samples. The primary elements are chromium, manganese, molybdenum, iron, nickel and silicon, with wt% values shown in Table 1. As mentioned above, the carbon and oxygen wt% values were omitted. Previous works of others, [1, 2] were used to verify this elemental composition and wt% values were consistent with 316 SS. The average wt% range found for 316 SS is shown in Table 2.

The pristine 316 SS element wt% values, determined by EDS, are within the lower and upper limit range, including standard deviations, or close enough to not suggest a significant difference. This provides confidence the untested 316 SS sample used is representative. The following section will analyze the fitting sample at point #1 and #2, mentioned above.

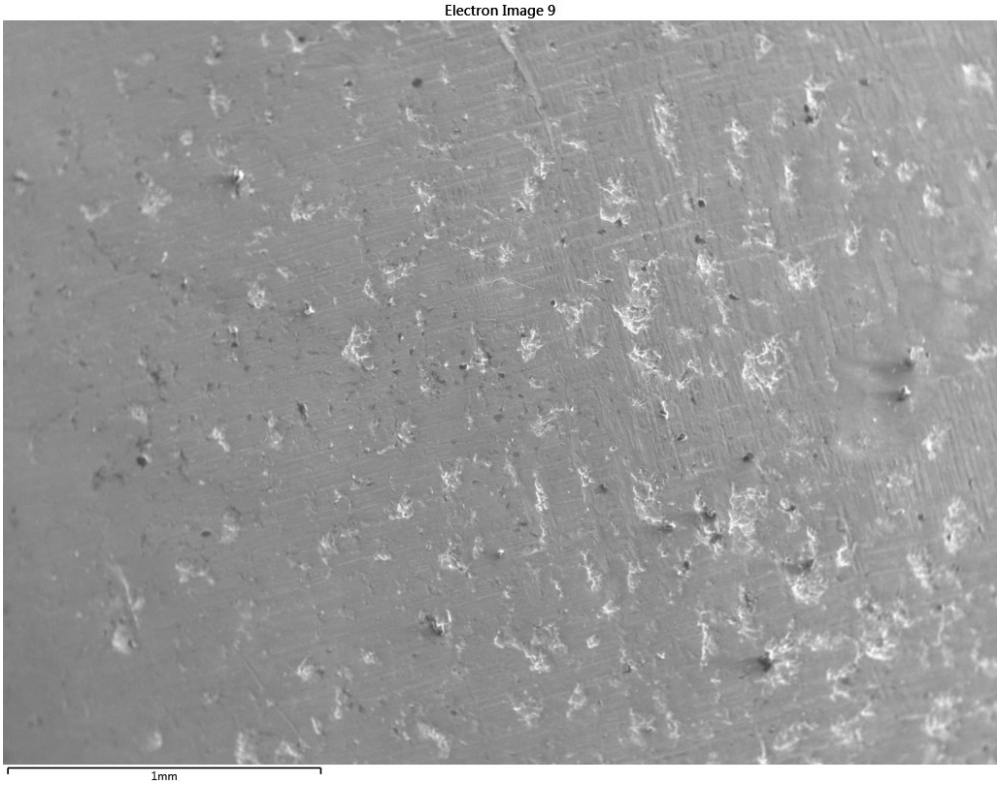

Figure 9: SEM Micrograph of the Pristine 316 SS Sample Surface

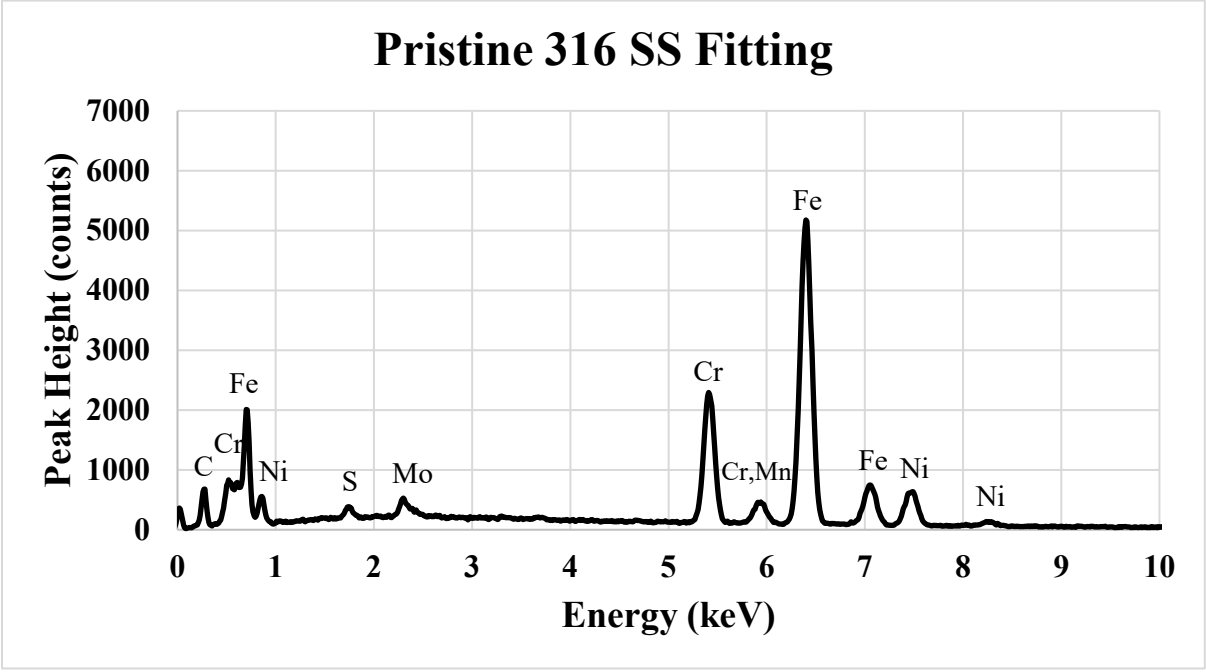

Figure 10: Raw EDS Results from Pristine 316 SS Fitting

Table 1: Pristine 316 SS Fitting Element Wt%

Element Type	Weight %
Chromium	15.17
Manganese	1.05
Molybdenum	2.23
Iron	63.00
Nickel	10.11
Silicon	0.57

Table 2: Reference Average 316 SS Elemental Composition Wt%

Element Type	Lower Limit Wt%	Upper Limit Wt%	Lower Limit SD	Upper Limit SD
Chromium	16.00	18.25	0.50	0.35
Manganese	1.00	2.00	1.41	0.00
Molybdenum	2.00	2.75	0.00	0.35
Iron	62.55	70.34	0.54	1.65
Nickel	10.00	13.50	0.00	0.71
Silicon	0.38	0.88	0.53	0.18

Figure 11 details the SEM micrograph for the interior cross-section cut of the 316 SS fitting sample. The micrograph details the interior metal (i.e., around the interior through hole) looks clean except for a few micro-cracks. The interior wall and part of the hole is filled with a material that appears porous. Both the interior wall and the interior metal were analyzed to determine their composition and compare with the pristine sample. The red circles show the locations that were analyzed.

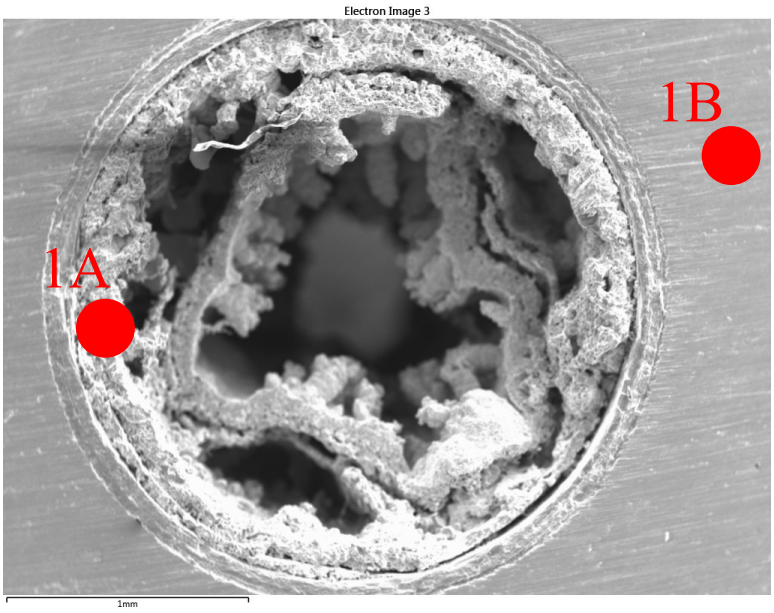

Figure 11: Cross-Section SEM Micrograph of the 316 SS Fitting

Figure 12 details the raw EDS results from the cross-section interior point #1A of the 316 SS sample fitting. The primary elements are chromium, manganese, sulfur, molybdenum, iron, nickel and silicon, with wt% values shown in Table 3. The first point noticed was that the center of the fitting has a significantly higher concentration of sulfur, which makes sense since high concentrations of H_2S were flowed through the fitting. The remaining elements are the same as before except many of the metals have lower concentrations, which are statistically outside the standard range for 316 SS. It is probable that the sulfur is reacting with the various metals and forming their respective metal-sulfide compound, or a multi-cation sulfide compound, which is then being eroded from the interior. While it is difficult to predict the exact chemical reactions that occurred, considering the high levels of sulfur and the high operating temperatures used, it is probable to hypothesize the lower metal concentrations are the result of metal-sulfide formation and/or metal-sulfide erosion from the surface, thus resulting in the lower metal wt% values.

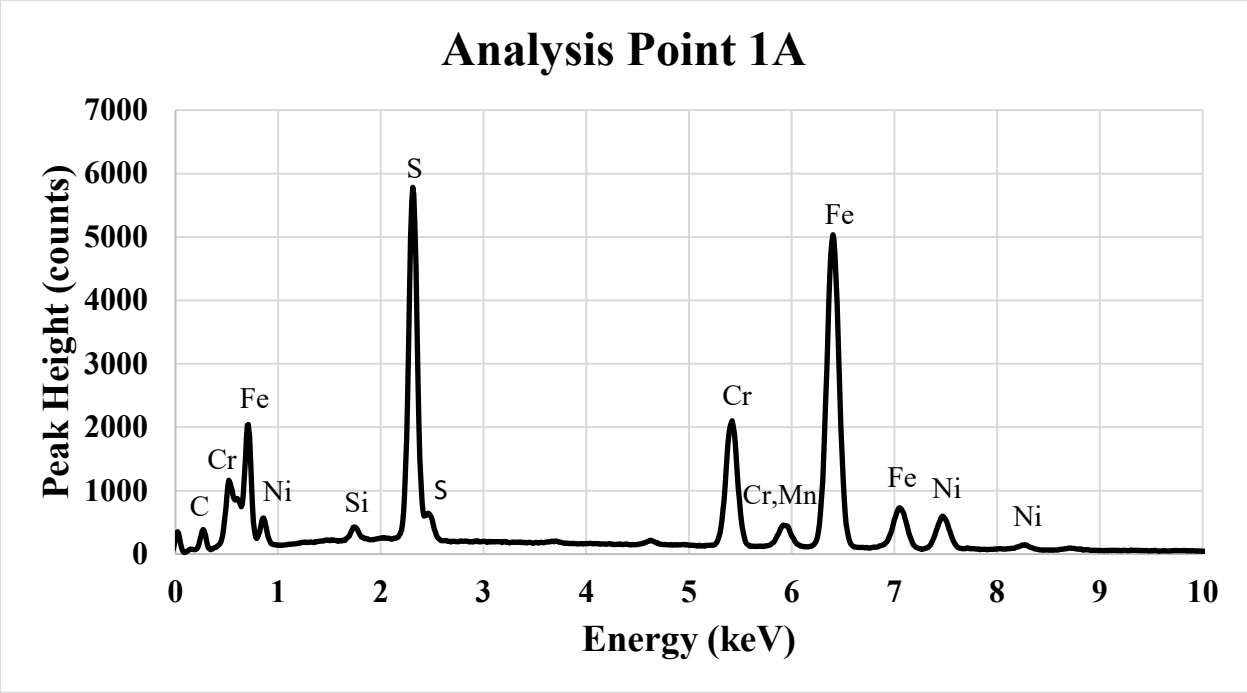

Figure 12: Raw EDS Results from 316 SS Fitting at Analysis Point 1A for the Fitting Interior Wall

Table 3: Cross-Section Point 1A for 316 SS Fitting Element Wt%

Element Type	Weight %
Chromium	14.64
Manganese	1.22
Sulfur	16.39
Molybdenum	1.74
Iron	56.15
Nickel	9.23
Silicon	0.63

Despite the high sulfur content, and lower metal elemental compositions, the interior is only 7.7-10.2% lower than the standard 316 SS composition, which is still similar. The largest concern observed is the physical restriction of gas through the fitting due to the deposition of this additional material.

Figure 13 details the raw EDS results from the cross-section interior point #1B of the 316 SS sample fitting. The primary elements are chromium, manganese, molybdenum, iron, nickel and silicon, with wt% values shown in Table 4. All the elements and their wt% values are statistically within the range provided in Table 2, which indicates heat-related diffusion of sulfur, or any other element occurred.

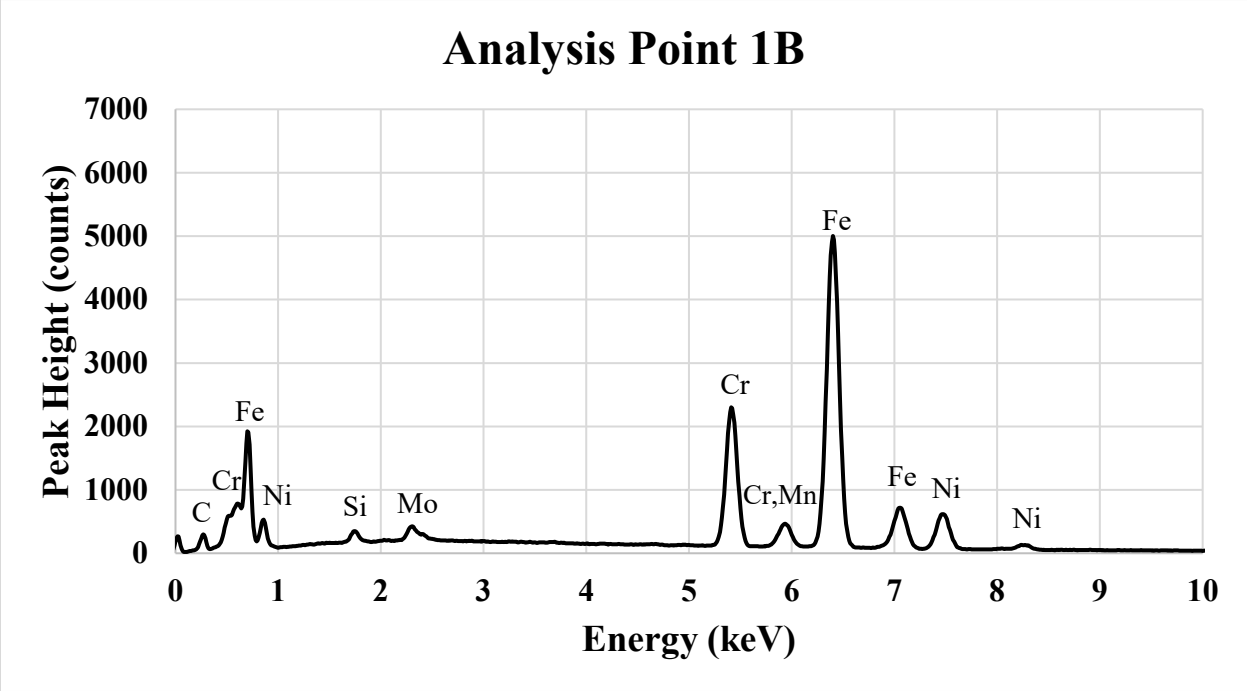

Figure 13: Raw EDS Results from 316 SS Fitting at Analysis Point 1B for the Fitting Interior Metal

Table 4: Cross-Section Point 1B for 316 SS Fitting Element Wt%

Element Type	Weight %
Chromium	18.23
Manganese	1.32
Molybdenum	2.06
Iron	65.66
Nickel	12.04
Silicon	0.70

Figure 14 details the SEM micrograph for the exterior surface of the 316 SS fitting sample. The surface is smooth and free from large defects, just like all the other metal surfaces.

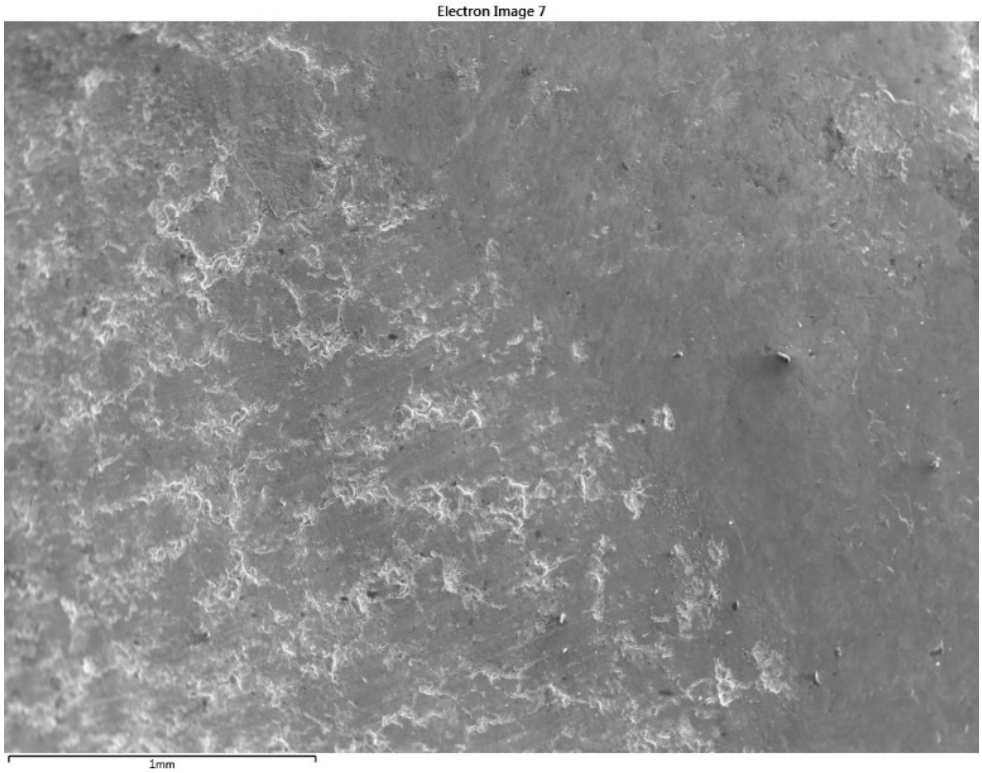

Figure 14: Exterior Surface SEM Micrograph of the 316 SS Fitting

Figure 15 details the raw EDS measurments from the exterior surface point #2 of the 316 SS sample fitting. The primary elements are chromium, manganese, molybdenum, iron, nickel, copper, and silicon, with wt% values shown in Table 5. All the elements appear to be close to their original values except for iron and nickel, which have significantly lower values. Since this is the outside surface, exposed to air, it is hypothesized those elements are being oxidized and over time being eroded away. This hypothesis is also supported by the high oxygen peak observed in Figure 15. The copper is most likely from the high-temperature copper-based anti-seize lubricant applied to the threads of the fitting during the original assembly. The iron and nickel have been reduced 42.2% and 24.4%, respectively, which is a sizeable loss and could lead to structure changes currently or in the future.

Figure 16 details the raw XRD measurements from both a pristine 316 SS sample (bottom) and the 316 SS fitting used for analysis points #1 and #2 (top), shown above. The contaminated fitting was analyzed across the cross-section cut where the interior (with metal-sulfide compounds) was exposed. The pristine sample had four peaks located at 43.54°, 44.52°, 50.74° and 74.08° 2θ. The miller indices, taken from literature [3], are shown below in Figure 16. Literature [3] also assigned the 44.52° peak as a combination of iron, chromium and nickel. Literature [3] does show that the 44.52° and 74.08° peaks can become diminished over time after a lengthy period of mechanical work has been applied.

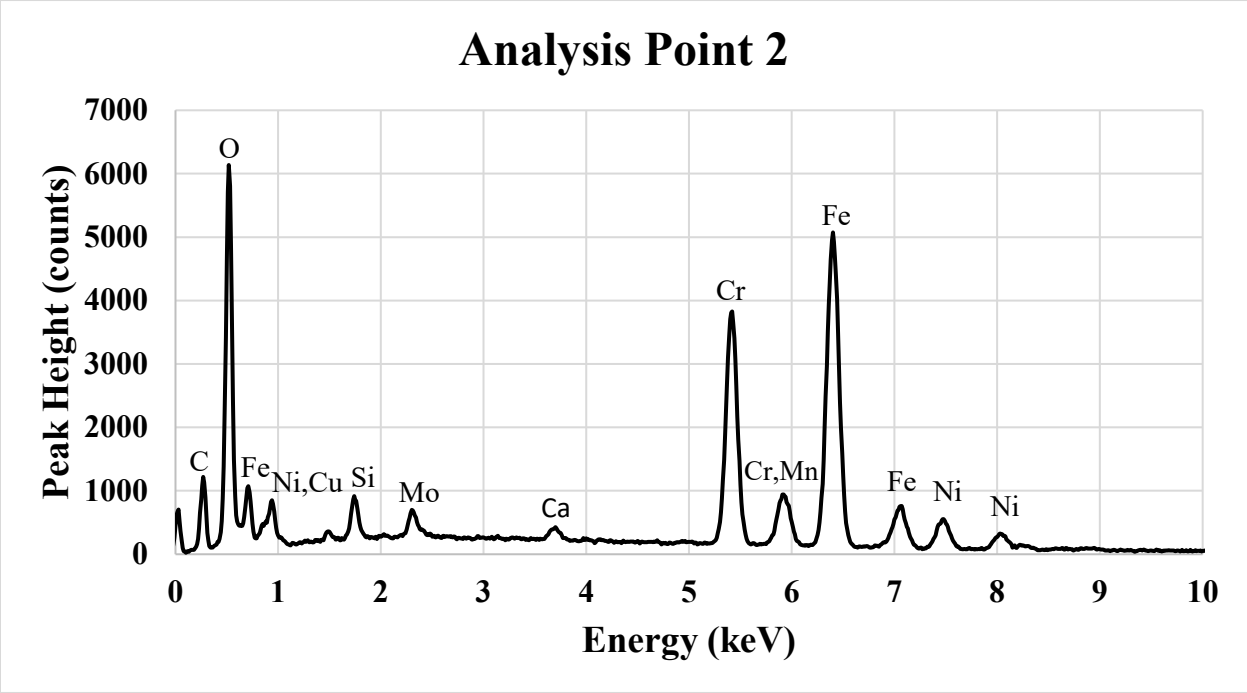

Figure 15: Raw EDS Results from 316 SS Fitting at Analysis Point #2 for the Fitting Exterior Surface

Table 5: Exterior Surface Point 2 for 316 SS Fitting Element Wt%

Element Type	Weight %
Chromium	16.65
Manganese	2.11
Molybdenum	2.25
Iron	36.16
Nickel	7.56
Silicon	0.93
Copper	2.94

The fitting sample had nearly the same peaks as the pristine sample except the 44.52° and 74.08° 2θ peaks were not visible, either because they were eliminated, or they became smaller than the background noise. The increased operating temperatures used in this paper could have resulted in the sample becoming more amorphous, as mechanical work does produce localized heat. Another possibility could be small amounts of contaminants diffused into the metal (undetectable to the EDS) and reduced the crystallinity of the sample. Overall, the peak intensity ratios between the remaining two peaks stayed close for both samples, so the overall material crystal structure stayed otherwise similar.

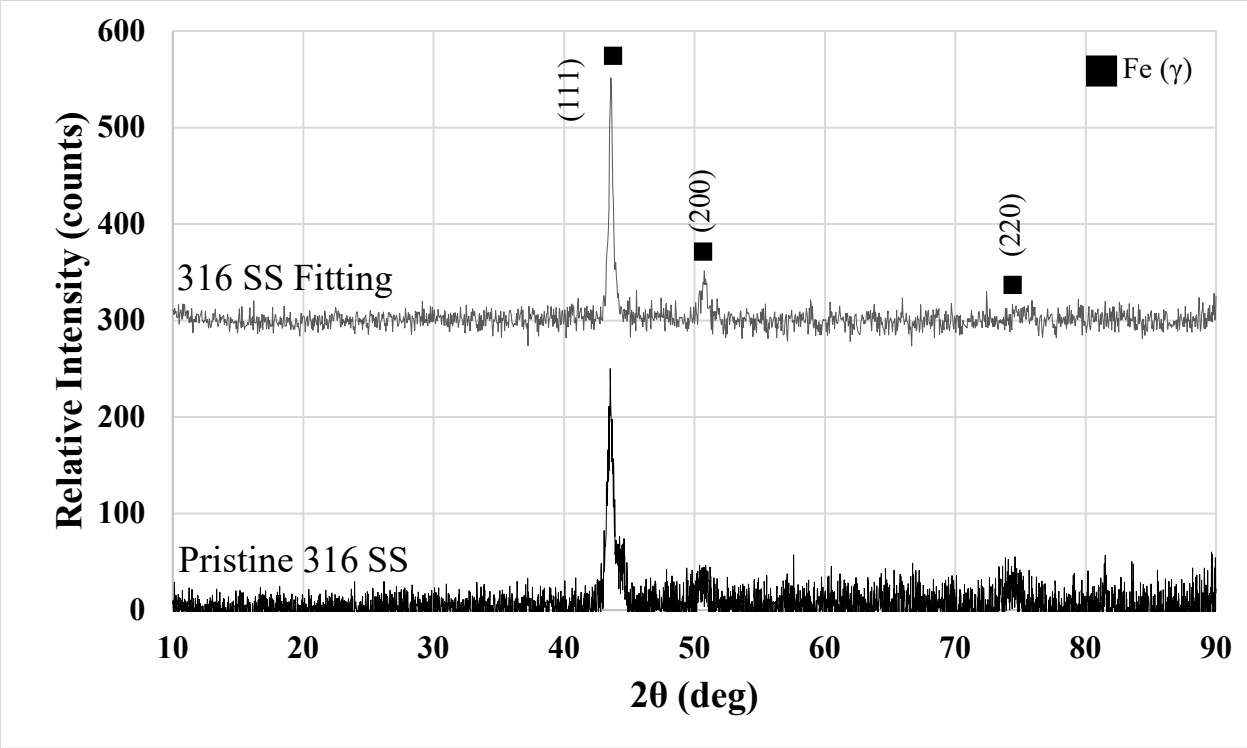

Figure 16: Raw XRD Results for Pristine 316 SS and Sample Fitting

3.1.2 316 SS Tube Results

Figure 17 details the SEM micrograph on the surface for the pristine 316 SS sample. The surface is clean of any large defects or pitting similar to what was shown for the pristine 316 SS fitting.

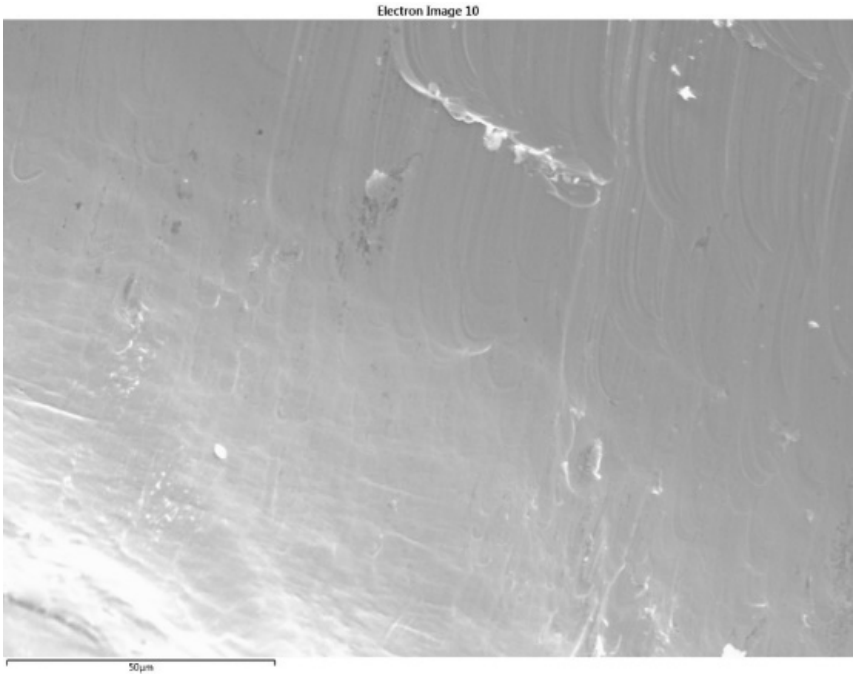

Figure 17: SEM Micrograph of the Pristine 316 SS Sample Surface

Figure 18 details raw EDS results from an untested 316 SS tube. This will also act as a baseline for the 316 SS tube. The primary elements are the same as with the pristine 316 SS fitting, which is to be expected. The exact wt% values for the pristine tube are shown in Table 6, which also are very similar to the wt% values in Table 1 and Table 2.

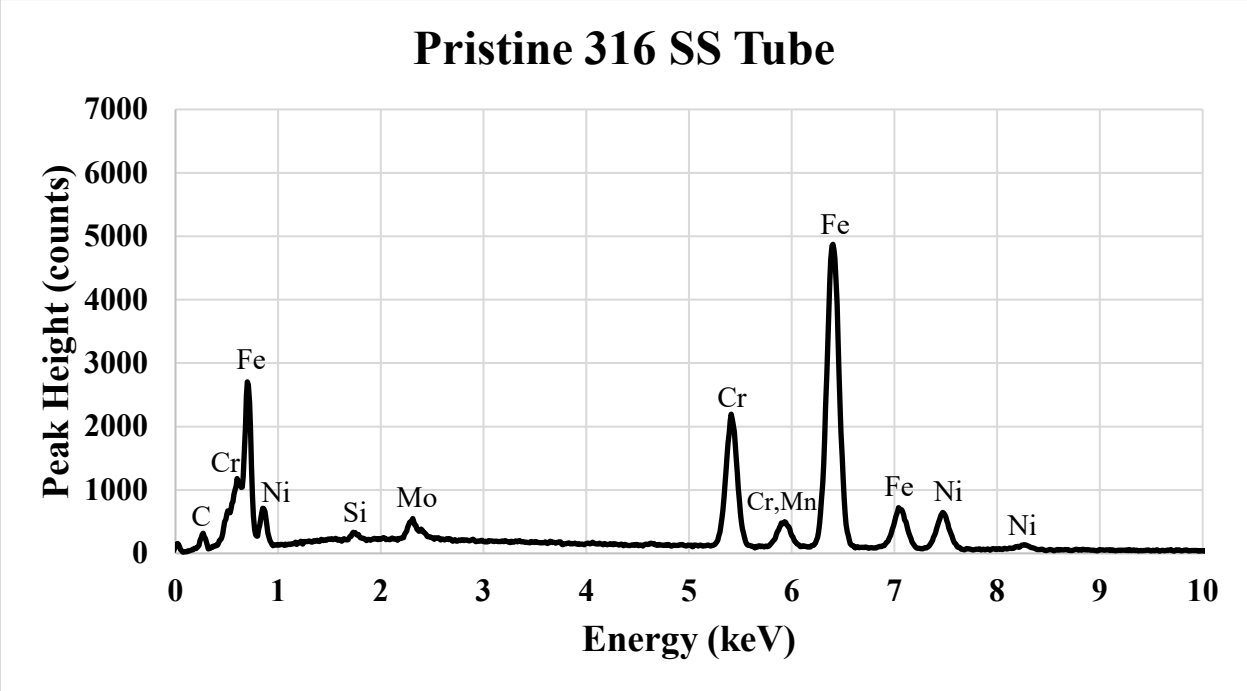

Figure 18: Raw EDS Results from Pristine 316 SS Tube

Table 6: Pristine 316 SS Tube Element Wt%

Element Type	Weight %
Chromium	16.23
Manganese	2.04
Molybdenum	2.67
Iron	61.87
Nickel	11.28
Silicon	0.43

Figure 19 details the SEM micrograph for the interior cross-section cut of the 316 SS tube sample. The surface is free of large defects and only has micro-scratches from the surface polishing. The two larger objects on the surface may be small pieces of dust but are not expected to impact the results.

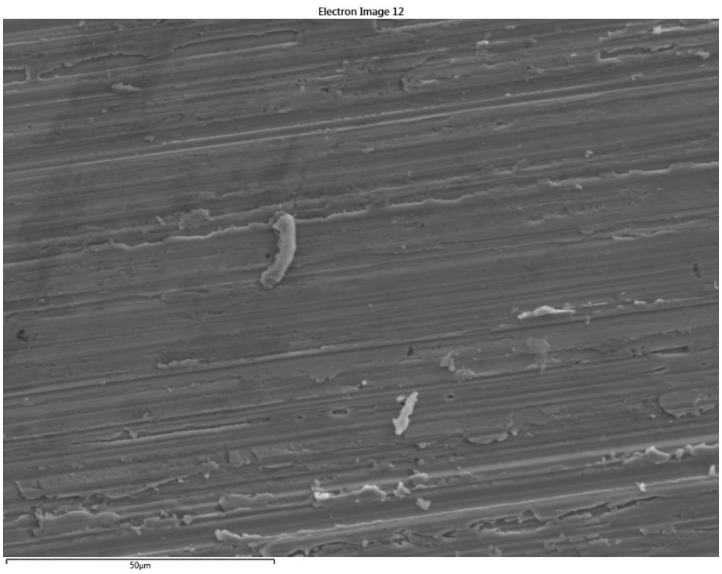

Figure 19: Cross-Section SEM Micrograph of the 316 SS Tube

Figure 20 details the raw EDS results from the cross-section interior point #3 of the 316 SS tube sample. The primary elements are chromium, manganese, molybdenum, iron, nickel and silicon, with wt% values shown in Table 7. The wt% values for all the elements are interestingly no different than the pristine 316 SS sample listed earlier. Despite the inlet tube being exposed to extremely high concentrations of H_2S at high temperatures, there does not appear to be elemental diffusion from the H_2S into the 316 SS tube or diffusion of the interior elements to the tube surface.

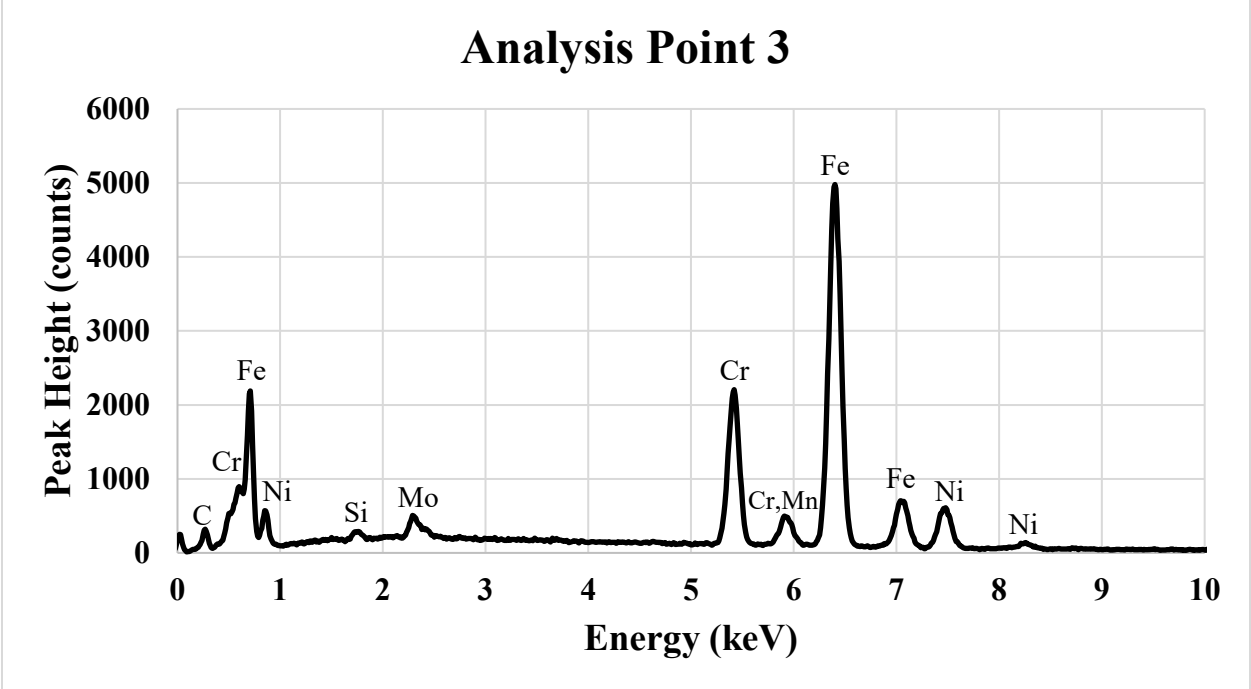

Figure 20: Raw EDS Results from 316 SS Tube at Analysis Point #3 for the Tube Interior Metal

Table 7: Cross-Section Point #3 for 316 SS Tube Element Wt%

Element Type	Weight %
Chromium	17.28
Manganese	1.92
Molybdenum	2.82
Iron	65.85
Nickel	11.67
Silicon	0.46

Figure 21 details the raw EDS results from the surface point #4 of the 316 SS tube sample. For this analysis point the exterior and interior surfaces of the tube are considered the same for the following reasons. First, the temperature gradient between the interior and exterior would be very small since the entire tube was inside the reactor. Second, the atmosphere would be the same for both surfaces since the H_2S gas concentration was very similar. The primary elements are chromium, manganese, sulfur, molybdenum, iron, nickel, silicon, lanthanum, strontium and vanadium, with wt% values shown in Table 8. The first thing to address is the presence of lanthanum, strontium and vanadium. Those elements are present on the surface since the tube was placed inside the LSV powder for optimal gas dispersal through the powder, so small amounts of those elements is expected. As observed previously there are a few metals that have lower wt% values, such as chromium, iron and nickel. Those were reduced by 42.3%, 30.8% and 53.2%, respectively. As observed with the 316 SS fitting, those elements, along with the high level of sulfur, are hypothesized to have formed a metal-sulfide surface layer.

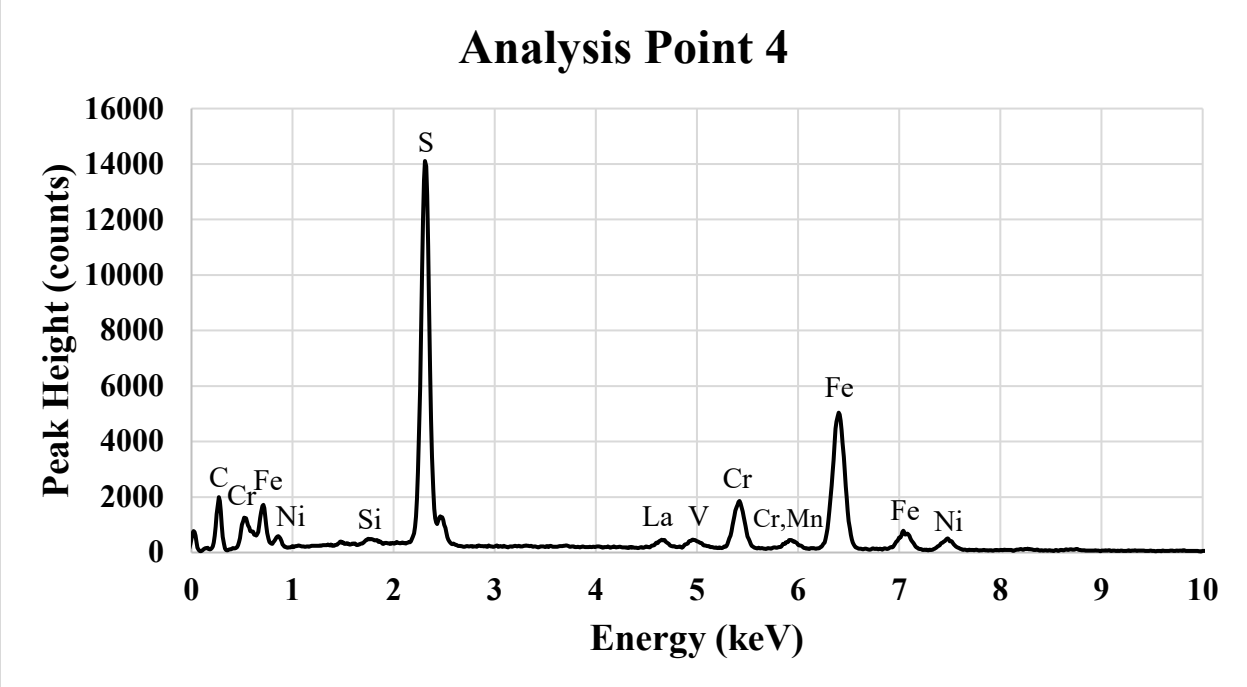

Figure 21: Raw EDS Results from 316 SS Tube at Analysis Point #4 for the Tube Surface

Table 8: Surface Point #4 for 316 SS Tube Element Wt%

Element Type	Weight %
Chromium	9.97
Manganese	0.99
Sulfur	32.43
Molybdenum	3.00
Iron	45.58
Nickel	5.46
Silicon	0.39
Lanthanum	2.76
Strontium	0.69
Vanadium	1.45

Figure 22 details the raw XRD results from both a pristine 316 SS sample (bottom) and the 316 SS tube used for analysis points 3 and 4 (top), shown above. Analysis of the tube, compared to the reference pristine 316 SS sample, was nearly identical as with the fitting sample. The only significant difference was the peak ratio between the 50.74° peak and the main peak increased, which indicates the sample was more amorphous than the fitting sample. This makes sense since the tube was exposed to higher temperatures inside the reactor compared to the fitting on the top of the lid, which was not directly heated by the heat tape.

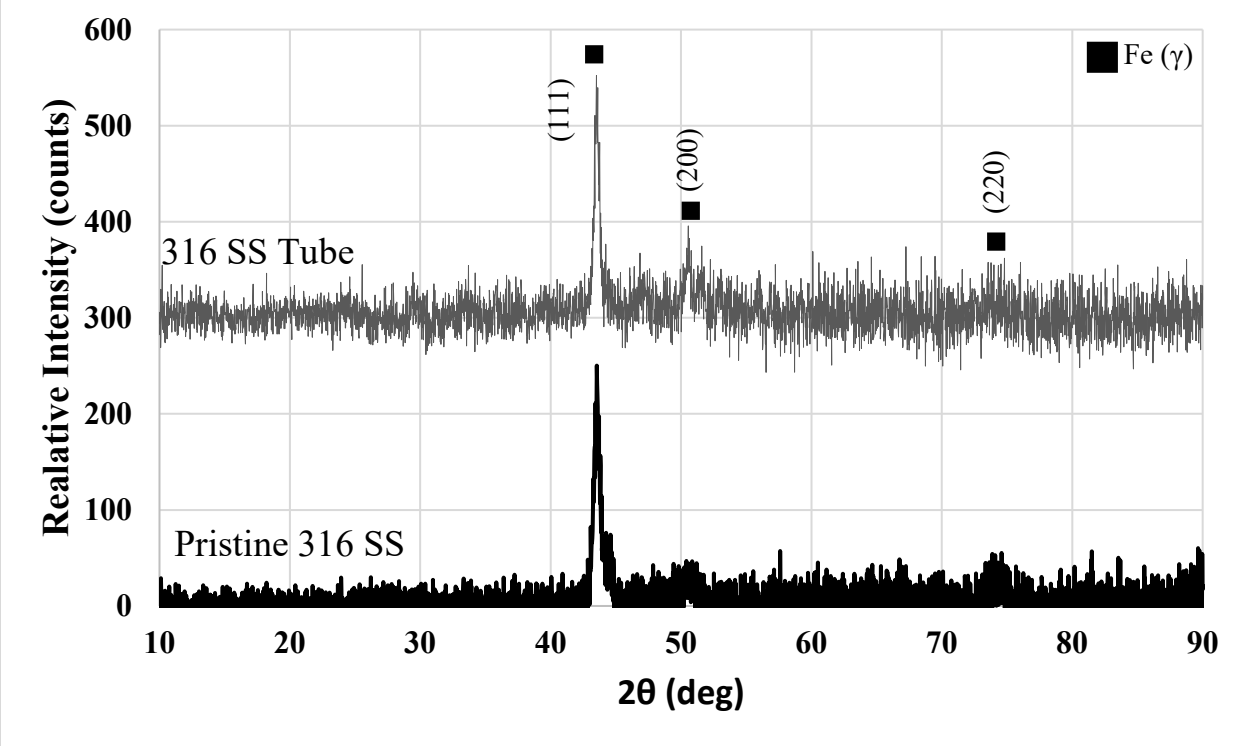

Figure 22: Raw XRD Results for Pristine 316 SS and Sample Tube

3.2 Inconel C-276 Characterization Results

This next section will discuss the Inconel C-276 metal used in the lid and body of the reactor. This material is much more resistant to corrosion, so material degradation is expected to be less, but still may have occurred and needs to be characterized.

3.2.1 Inconel C-276 Lid Results

Initially, a pristine untested Inconel C-276 sample was characterized using EDS and XRD to establish a baseline.

Figure 23 details the SEM micrograph on the surface for the pristine Inconel C-276 sample. As with the other samples its surface is free of large defects or large deposits, which could influence the results.

Figure 24 details raw EDS results from an untested Inconel C-276 sample. This baseline examines significant elemental changes which may have occurred in samples. The primary elements are chromium, molybdenum, nickel and iron, with smaller amounts of manganese and tungsten. The actual wt% values are shown in Table 9. As mentioned above, the carbon and oxygen wt% values were omitted in Table 9. These values fall within or are very similar to the reported elemental composition for Inconel C-276 from industry manufactures or online material databases [4, 5].

Table 10 details the element composition range reported online for pristine Inconel C-276. Comparing the elemental composition calculated from Figure 24 (reported in Table 9) against these reported values details the pristine Inconel sample is the same.

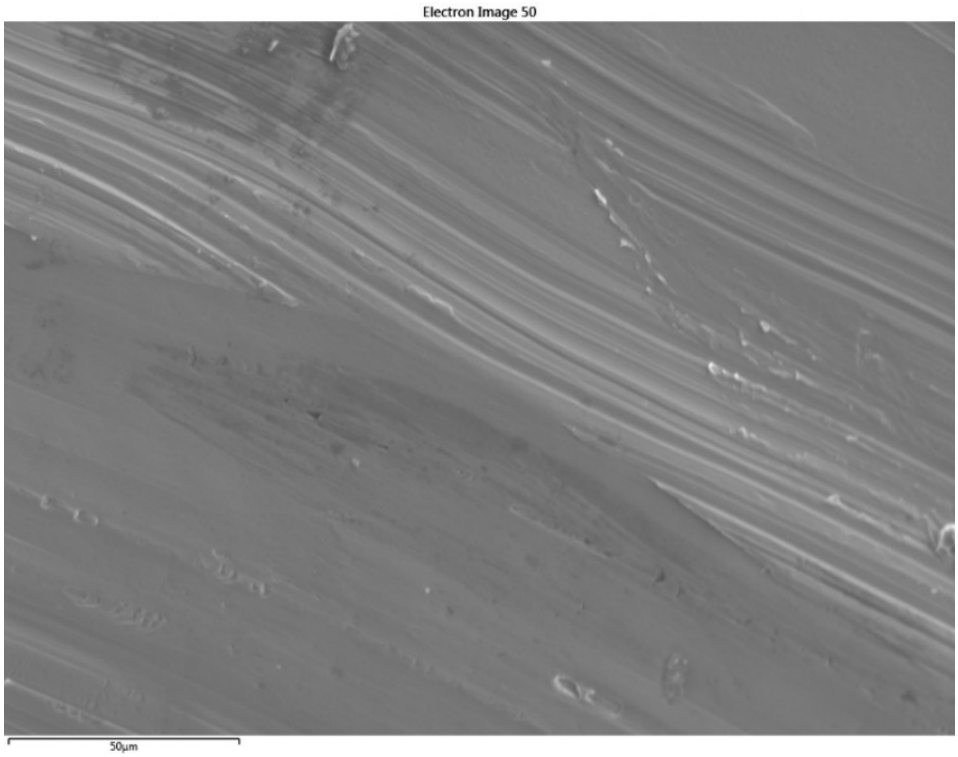

Figure 23: SEM Micrograph of the Pristine Inconel C-276 Sample Surface

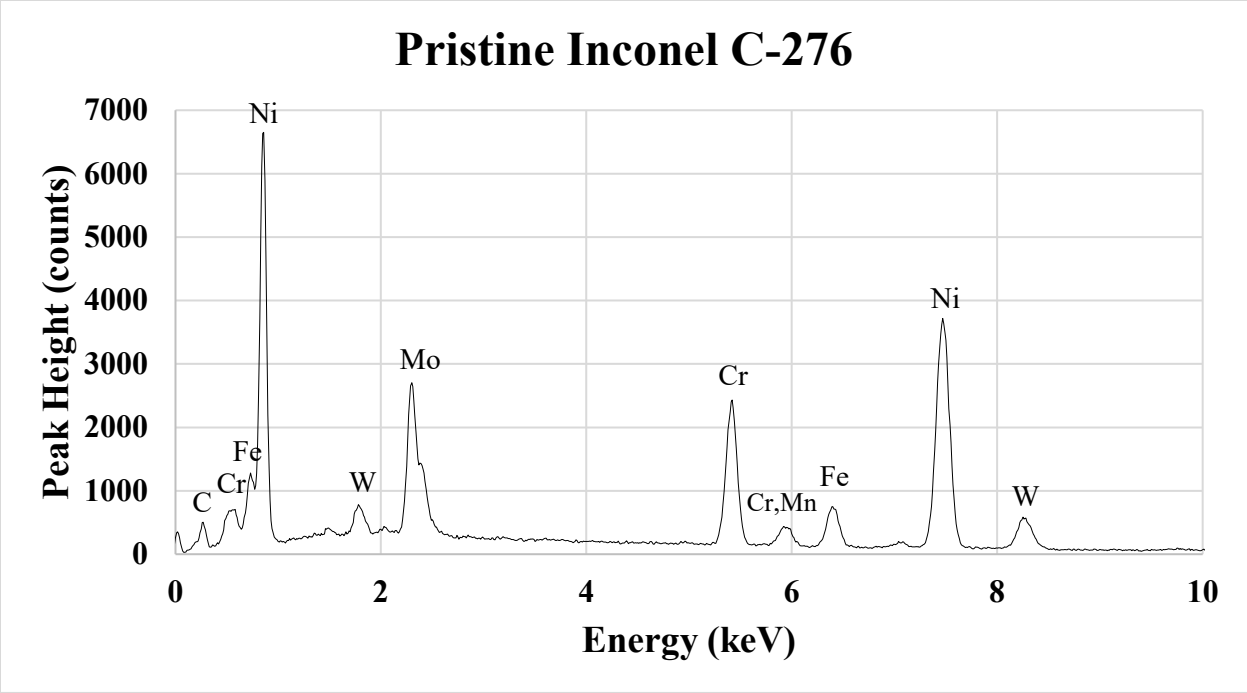

Figure 24: Raw EDS Results from Pristine Inconel C-276

Table 9: Pristine Inconel C-276 Element Wt%

Element Type	Weight %
Silicon	0.00
Chromium	16.32
Manganese	0.41
Phosphorus	0.00
Nickel	58.03
Molybdenum	14.63
Iron	6.34
Cobalt	0.00
Vanadium	0.00
Sulfur	0.00
Tungsten	3.72

Figure 25 details the raw XRD results for the pristine Inconel C-276. The peaks are from nickel and the (111) peak is the most intense peak. While the peaks shown below are fairly well defined their intensity is lower than other pure Inconel studies found in literature. The lower peak intensity values found in the pristine reference, shown here, was probably due to either a smaller sample size used or a shorter scanning duration, compared to samples found in literature. All samples in this study were characterized using XRD for 40 minutes, which is typically adequate. Otherwise, this XRD data is consistent with other literature studies for peak positions and peak intensity ratios.

Table 10: Reference Average Inconel C-276 Elemental Composition Wt%

Element Type	Lower Limit Wt%	Upper Limit Wt%
Silicon	0.00	0.08
Chromium	14.50	16.50
Manganese	0.00	1.00
Phosphorus	0.00	0.04
Nickel	50.99	69.50
Molybdenum	15.00	17.00
Iron	4.00	7.00
Cobalt	0.00	2.50
Vanadium	0.00	0.35
Sulfur	0.00	0.03
Tungsten	3.00	4.50

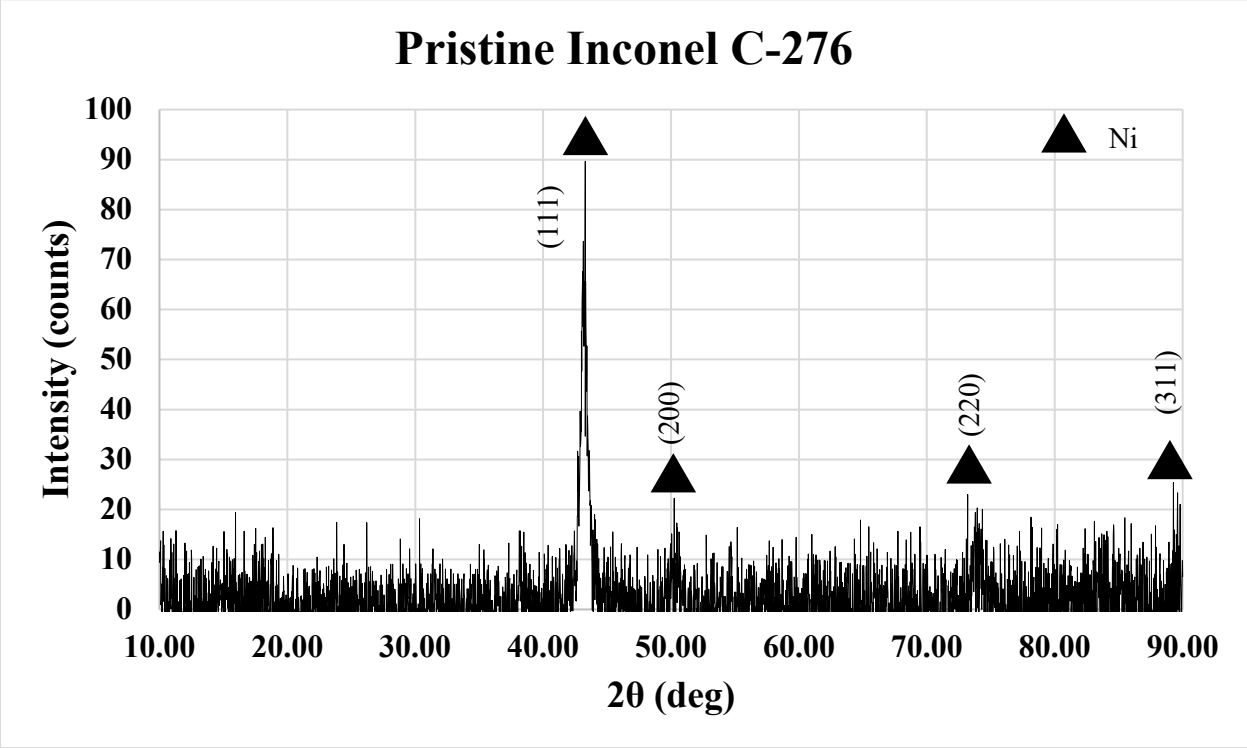

Figure 25: Raw XRD Results for Pristine Inconel C-276

Figure 26 details the SEM micrograph for the outer edge of the Inconel lid sample at analysis point #11. The outer surface has many pits and other surface defects, which could be the result of an oxide coating forming or other chemical deposits. It clearly is not as clean as the pristine sample.

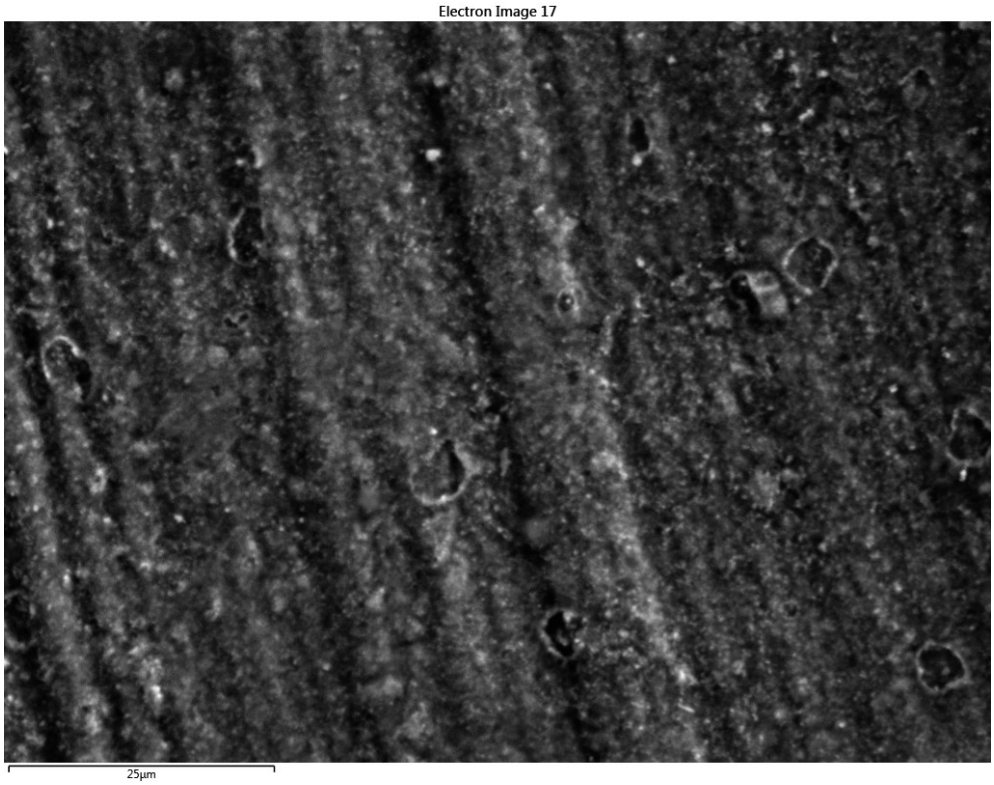

Figure 26: Outer Edge SEM Micrograph of Inconel Lid

Figure 27 details the raw EDS results from the outer edge analysis point #11 of the Inconel lid sample. There are similar primary elements present as the pristine sample, but in noticeably different amounts, shown in Table 11. The first noticeable difference is the significantly elevated chromium, silicon, and oxygen peaks. As stated earlier the exact oxygen wt% value cannot be accurately determined but combined with the SEM image which appears to have a coating, it is hypothesized an oxide coating formed on the sample. This may be chromium oxide or silicon oxide (due to the elevated chromium and silicon) or the chromium and silicon may have simply diffused to the surface. Other possibilities for the elevated silicon are either the insulation or heat tape wrapped around the reactor may have silicon that diffused to the metal surface. Both the insulation and heat tape will be evaluated for elemental silicon at the end of Section 3. Finally, presence of copper is either from the copper tape used to hold the sample to the SEM stage or the copper-based anti-seize lubricant, previously mentioned.

Even though the chromium is 3.62x higher than the untested sample the silicon is more concerning since only a maximum of 0.08 wt% is in Inconel. The silicon in this sample is 8.63x higher and could be forming a thermal and/or electrically resistive coating, which will require further analysis outside this study. The second difference is the significantly lower amounts of nickel and molybdenum. Even the iron is slightly lower than the pristine sample. These changes to the elemental composition could indicate significant material property changes if these results are found throughout the entire lid. The other samples need to be analyzed to determine if this is simply a surface effect.

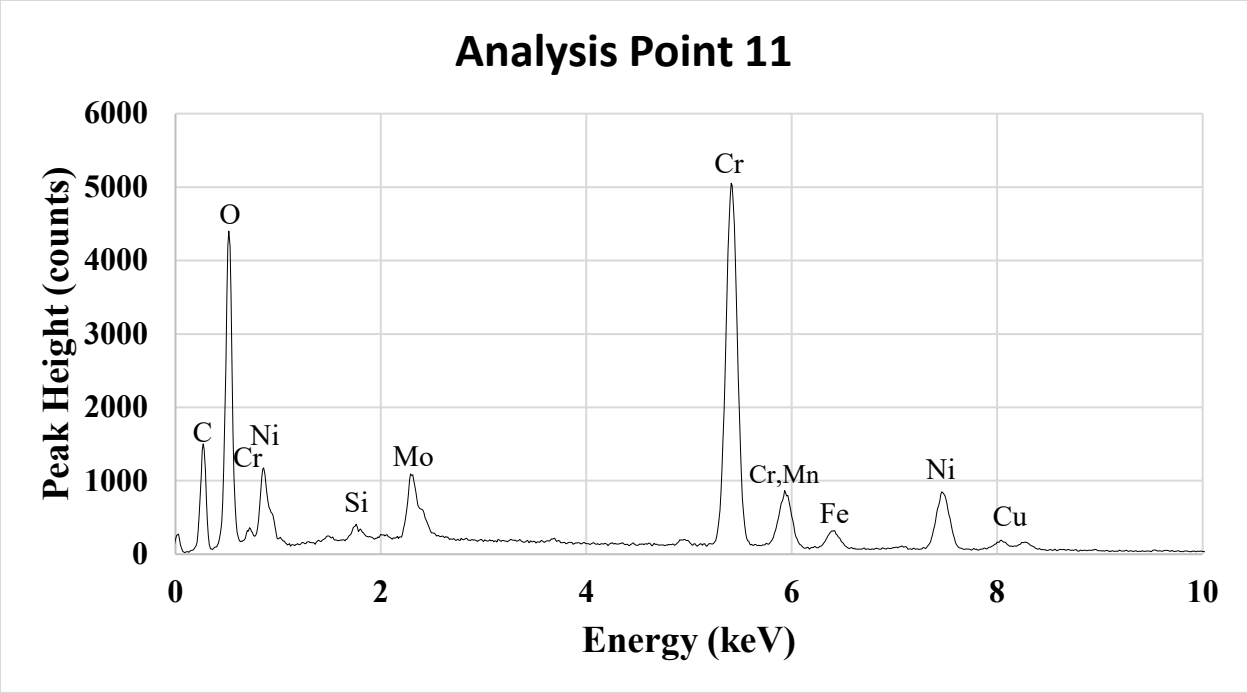

Figure 27: Raw EDS Results from Inconel Lid at Analysis Point 11 for the Outer Edge

Table 11: Outer Edge Point 11 for Inconel Lid Element Wt%

Element Type	Weight %
Silicon	0.69
Chromium	58.88
Manganese	1.98
Phosphorus	0.00
Nickel	20.35
Molybdenum	10.05
Iron	4.33
Cobalt	0.00
Vanadium	0.00
Sulfur	0.00
Tungsten	0.00

Figure 28 details the raw XRD results from both a pristine Inconel sample (bottom) and the outer edge used for analysis point #11, shown above. Analysis point #11 is similar to the untested sample, but does have two noticeable differences. First, the peak positions shifted to a slightly lower 2θ position, which indicates their lattice parameters changed. This is not surprising considering the change in elemental composition shown with the EDS results. Second, the (200) peak has considerably higher intensity compared to the pristine sample.

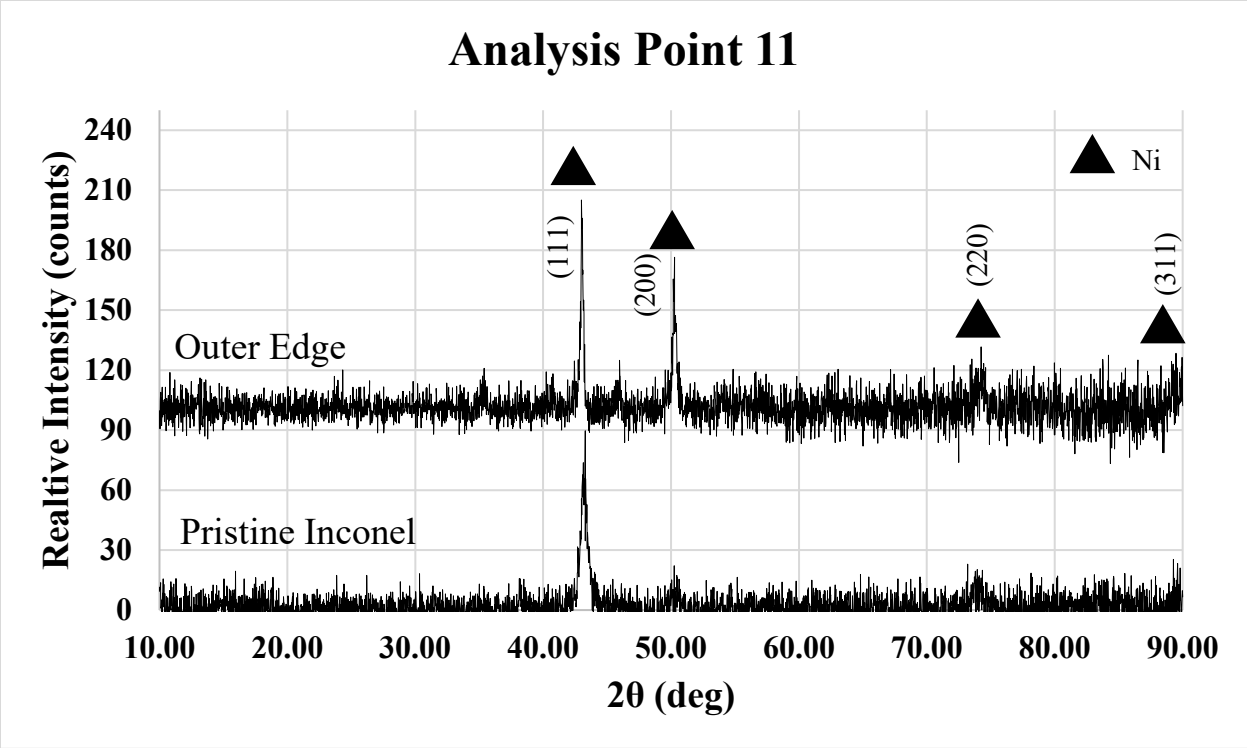

Figure 28: Raw XRD Results for Pristine Inconel and Outer Edge Sample

The following figures show the combined SEM, EDS and XRD results from analysis points #8, 9 and 10 since they all were taken from the same radial position with just different sample depths. Figure 29 details the SEM micrographs for the Inconel lid sample at analysis point #8 (left), #9 (middle) and #10 (right). Analysis point #8 is from the top surface and also details a coating of some type. Analysis point #9 was located in the center of the lid and appears smooth with small lines from the cutting saw. Finally, analysis point #10 is from the underside of the lid where a vermiculite seal was used and where the sulfur and LSV powder were exposed to the Inconel. The surface is coated with a large number of rough deposits.

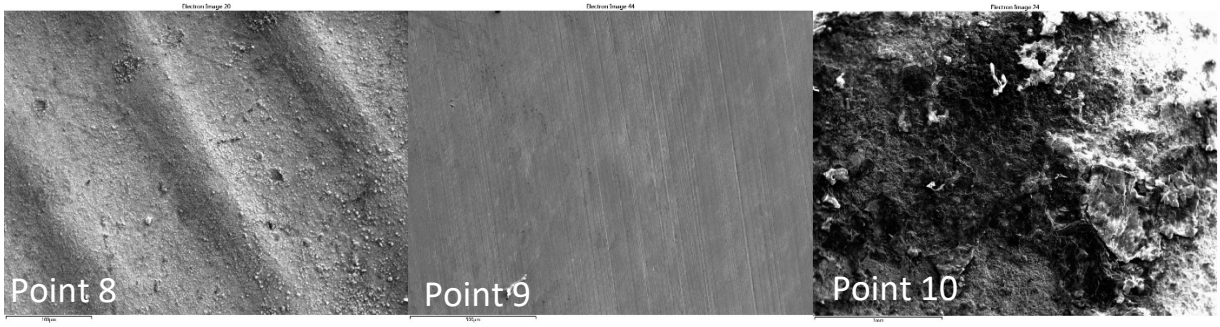

Figure 29: Analysis Points #8 (left), #9 (middle) and #10 (right) SEM Micrograph of Inconel Lid

Figure 30 details the raw EDS results from the analysis points #8 (top), #9 (middle) and #10 (bottom). The wt% values calculated from these samples are shown below in Table 12. The top showed similar results with the outer edge sample, such as elevated oxygen, chromium, and

silicon. Point #9 had elemental concentrations that were consistent with the pristine Inconel sample, which details the contaminants or high operating temperatures did not elementally change the interior of this radial position. Point #10 at the bottom is a mixture of multiple elements and is very difficult to separate. The high silicon, magnesium and iron are consistent with the composition of the vermiculite used in the seal between the body and lid. The lower concentrations of nickel, chromium and molybdenum are hypothesized to be from the vermiculite masking those elements in the Inconel.

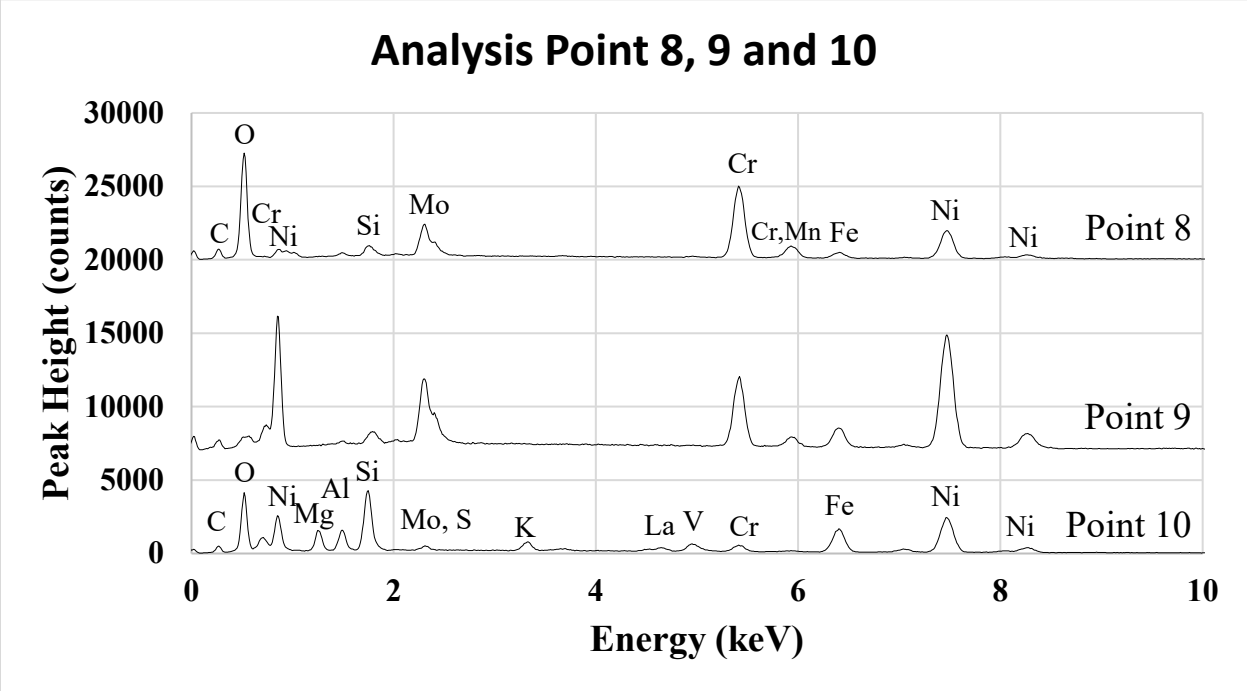

Figure 30: Raw EDS Results from Inconel Lid at Analysis Point #8, #9 and #10

Table 12: Analysis Point #8, #9 and #10 for Inconel Lid Element Wt%

Element Type	Point 8 Weight %	Point 9 Weight %	Point 10 Weight %
Silicon	1.96	0.00	9.05
Chromium	40.90	16.22	1.87
Manganese	2.08	0.40	0.23
Phosphorus	0.00	0.00	0.00
Nickel	33.41	55.99	28.92
Molybdenum	17.07	16.69	0.00
Iron	4.64	6.28	12.25
Cobalt	0.00	0.06	0.00
Vanadium	0.00	0.00	2.35
Sulfur	0.00	0.00	0.63
Tungsten	0.00	3.91	0.00

Figure 31 details the raw XRD results from analysis points #8 (top), #9 (middle) and #10 (bottom). The pristine sample XRD results were omitted from this plot since their peaks would be difficult to view with the expanded y-axis. The bottom (point #10) only details the vermiculite and none of the Inconel, so further surface analysis could not be conducted there. The top (point #8) and middle (point #9) both had similar peak ratio values between the (111) and (200) peaks, compared to the pristine sample, unlike the outer edge. However, the (220) and (311) peaks were either not present (point #8) or their peak intensities were diminished compared to the (111) peak (point #9). The increased operating temperature could have changed the lattice parameters and/or the altered elemental composition on the surface may have impacted the top and center locations. Overall, the structure at these points is still very close to the pristine sample.

The following figures now will investigate the center of the lid radially using different depths in a similar fashion as conducted above showing the combined SEM, EDS and XRD results from analysis points #5, #6 and #7. Figure 32 details the SEM micrographs for the Inconel lid sample at analysis point #5 (right), #6 (middle) and #7 (right). As with analysis points #8, #9 and #10 the top and bottom show a deposited coating and the middle is a relatively clean surface. The bottom surface deposits look more granular, which is probably from vermiculite not being used here.

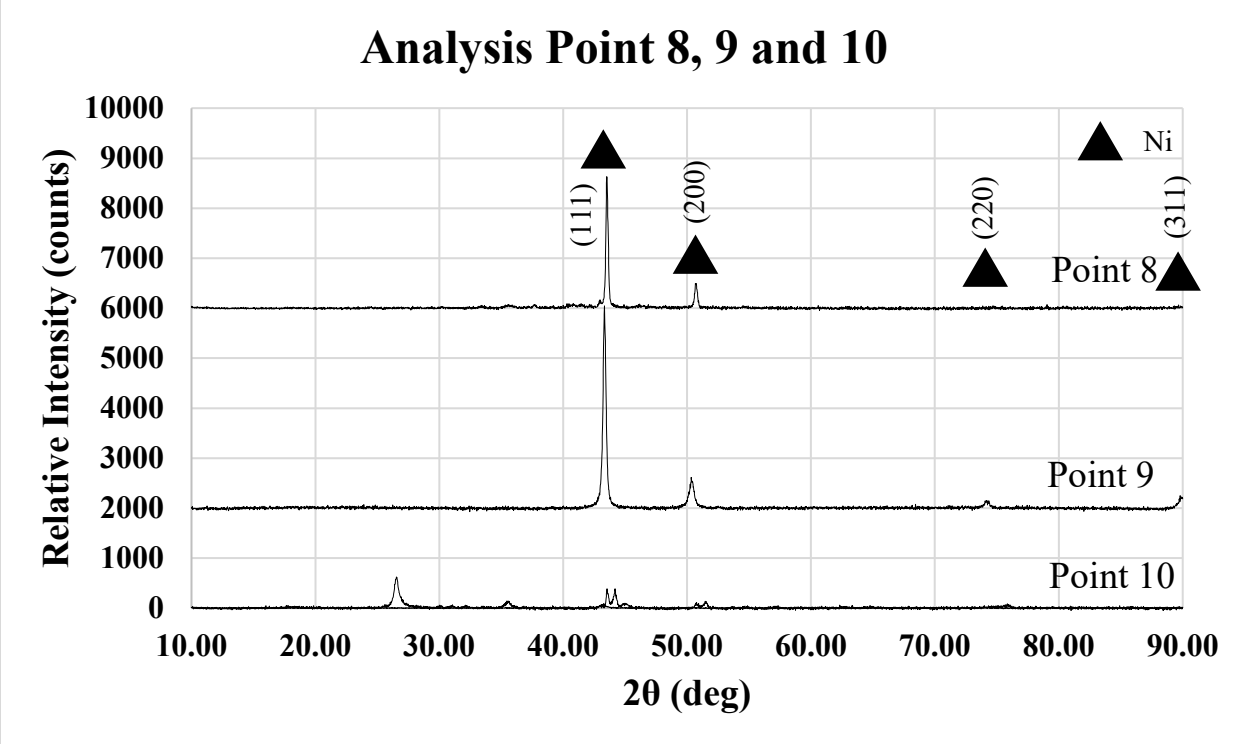

Figure 31: Raw XRD Results Analysis Points 8,9 and 10

Figure 32 details the SEM micrographs for the Inconel lid sample at analysis point #5 (right), #6 (middle) and #7 (right). These three SEM micrographs have a similar appearance to the point #8, #9 and #10 micrographs in that the top surface (points #5 and #8) show a coating, the center (point #6 and #9) is a clean metal surface and the bottom surface (points #7 and #10) have a thick layer of deposited material. The largest difference between these images is the bottom surface coating,

where the coating in point #7 does not contain vermiculite. The coating in Figure 32 is more granular and appears more evenly distributed.

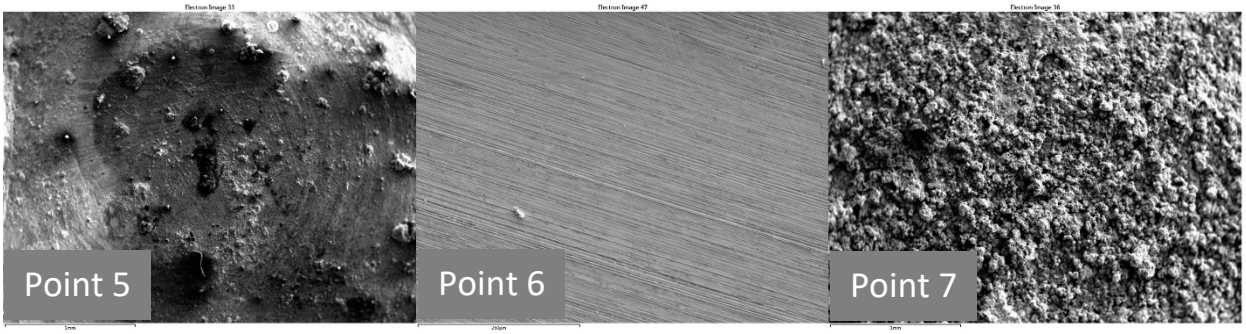

Figure 32: Analysis Points #5 (left), #6 (middle) and #7 (right) SEM Micrograph of Inconel Lid

Figure 33 details the raw EDS results from the analysis points #5 (top), #6 (middle) and #7 (bottom). The wt% values calculated from these samples are shown below in Table 13. These results, again, are similar to the EDS analysis of points #8, #9 and #10. Similarities between both datasets can be seen through both top surfaces are dominated by oxygen and chromium, while the center is similar to the pristine Inconel sample. There are differences, which include copper on the top surface and high sulfur content (instead of an oxygen/silicon rich surface) on the bottom. The copper is attributed from the anti-seize compound used for the 316 stainless steel fittings, and the sulfur is from the H_2S gas used.

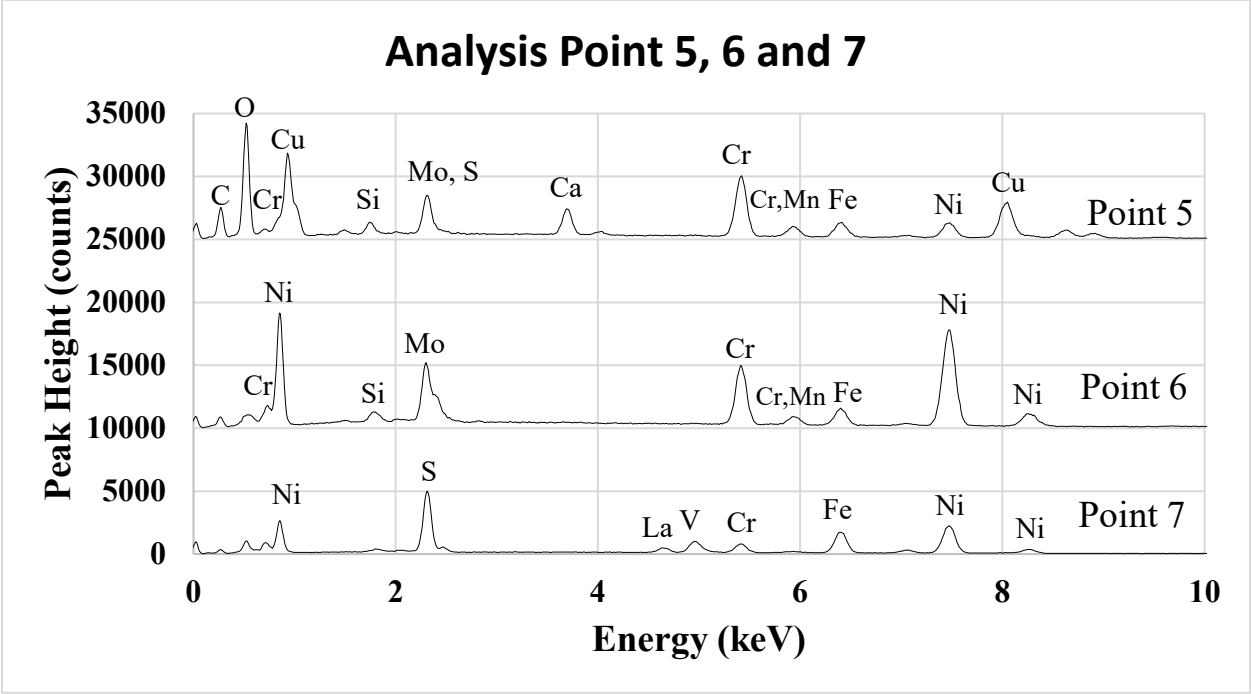

Figure 33: Raw EDS Results from Inconel Lid at Analysis Point #5, #6 and #7

Table 13: Analysis Point #5, #6 and #7 for Inconel Lid Element Wt%

Element Type	Point 8 Weight %	Point 9 Weight %	Point 10 Weight %
Silicon	1.31	0.00	0.00
Chromium	16.75	16.16	4.42
Manganese	1.01	0.44	0.46
Phosphorus	0.00	0.00	0.00
Nickel	8.58	55.80	40.56
Molybdenum	1.93	16.35	0.67
Iron	5.46	6.23	20.34
Cobalt	0.13	0.10	0.16
Vanadium	0.00	0.18	6.33
Lanthanum	0.00	0.00	6.57
Strontium	0.00	0.00	1.27
Sulfur	3.58	0.00	17.30
Tungsten	0.00	4.03	3.86
Copper	26.20	0.00	0.72

Figure 34 details the raw XRD results from analysis points #5 (top), #6 (middle) and #7 (bottom). Overall, the results here are very similar to the XRD results shown in Figure 31. Differences between points #7 and #10 is the former did not have vermiculite, but was exposed to sulfur, and the latter had vermiculite and less sulfur. Peaks were not labeled since there are many possible compounds present and would be difficult to separate.

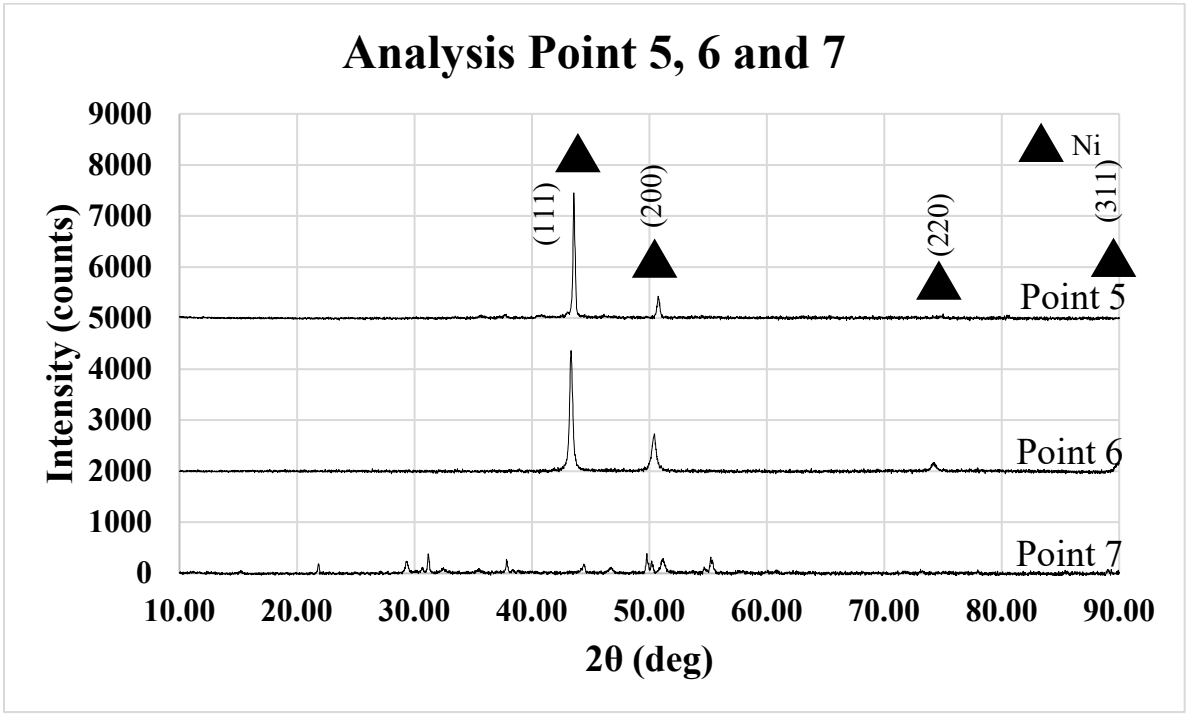

Figure 34: Raw XRD Results Analysis Points 5,6 and 7

3.2.2 Inconel C-276 Body Results

Figure 35 details the SEM micrographs for the Inconel body outer wall sample at analysis point #12. The outer wall surface appears to have a coating or even a scale, which in itself is not much different from the other samples exposed to air. The primary difference here is the scale is not as uniform as coatings on the other samples. Analysis using the EDS and XRD provides more information.

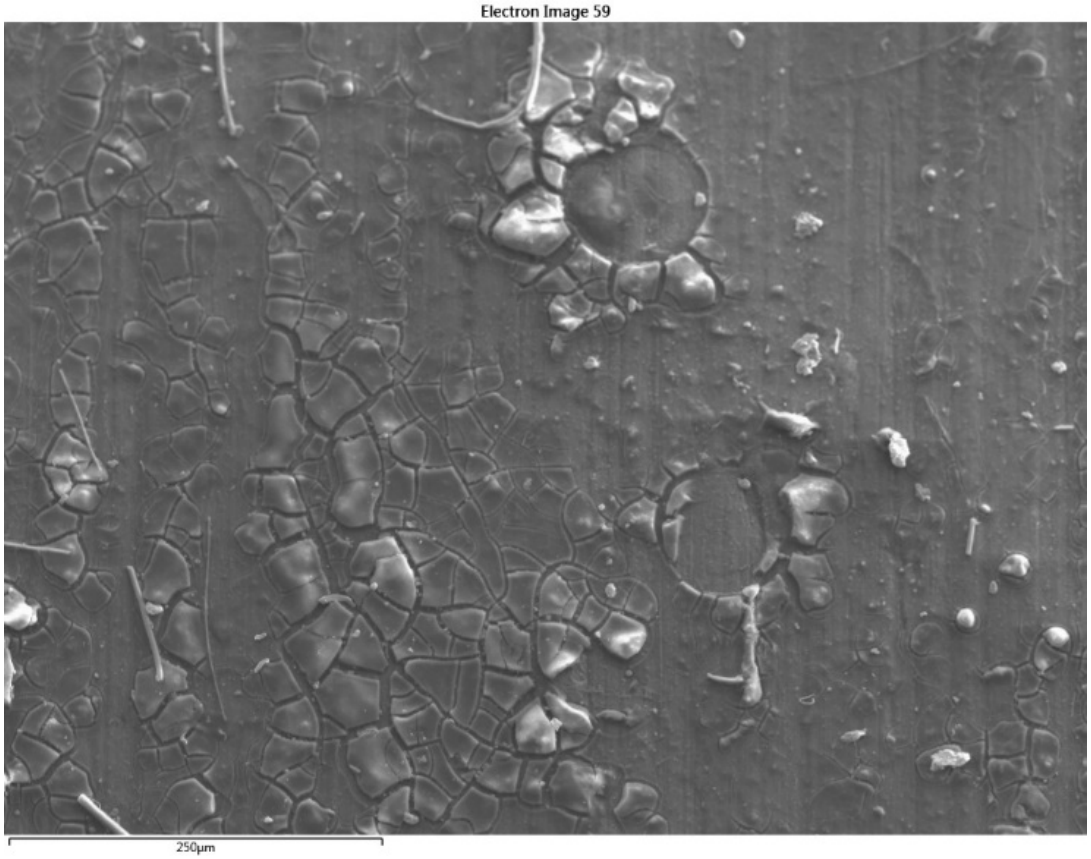

Figure 35: Analysis Points 12 SEM Micrograph of Inconel Body Outer Wall

Figure 36 details the raw EDS results from analysis point #12. The wt% values calculated from these samples are shown below in Table 14. Unlike with the previous samples exposed to air this surface has significantly higher levels of silicon than before. The chromium is still significantly elevated from the pristine Inconel sample, but the silicon here dominates. The coating observed in the SEM image is very likely a silicate of some type or simply silicon dioxide.

Figure 37 details the raw XRD results from analysis point #12. This is the first sample where the surface coating registered as separate peaks on the XRD scan, which is interesting. This details that while the peak intensity is not large, the results are well defined, and thus the coating must have crystallinity. As well, the peaks from Inconel are not present so this coating must be blocking the metal underneath. Attempts at matching the reference database to the coating XRD scan did not find any matches. It is likely a silicate compound that is not in the database due to the large number of elements present in Inconel which the silicon could have reacted with.

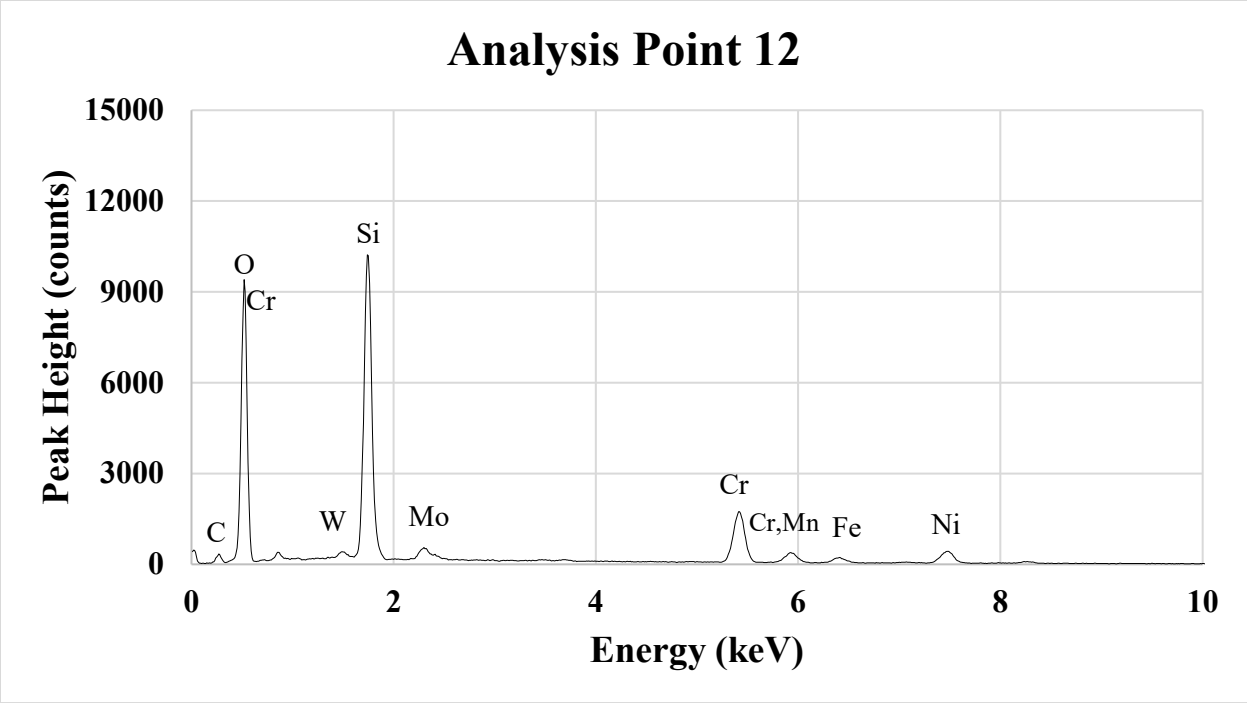

Figure 36: Raw EDS Results from Inconel Body Outer Wall at Analysis Point #12

Table 14: Analysis Point #12 for Inconel Body Element Wt%

Element Type	Point 8 Weight %
Silicon	46.92
Chromium	25.70
Manganese	2.13
Phosphorus	0.00
Nickel	12.63
Molybdenum	6.24
Iron	3.64
Cobalt	0.00
Vanadium	0.16
Tungsten	1.04

Figure 38 details the SEM micrographs for the Inconel body center sample at analysis point #13. As with all the other center location samples this does not show any irregular deposits or markings other than the marks from the cutting saw.

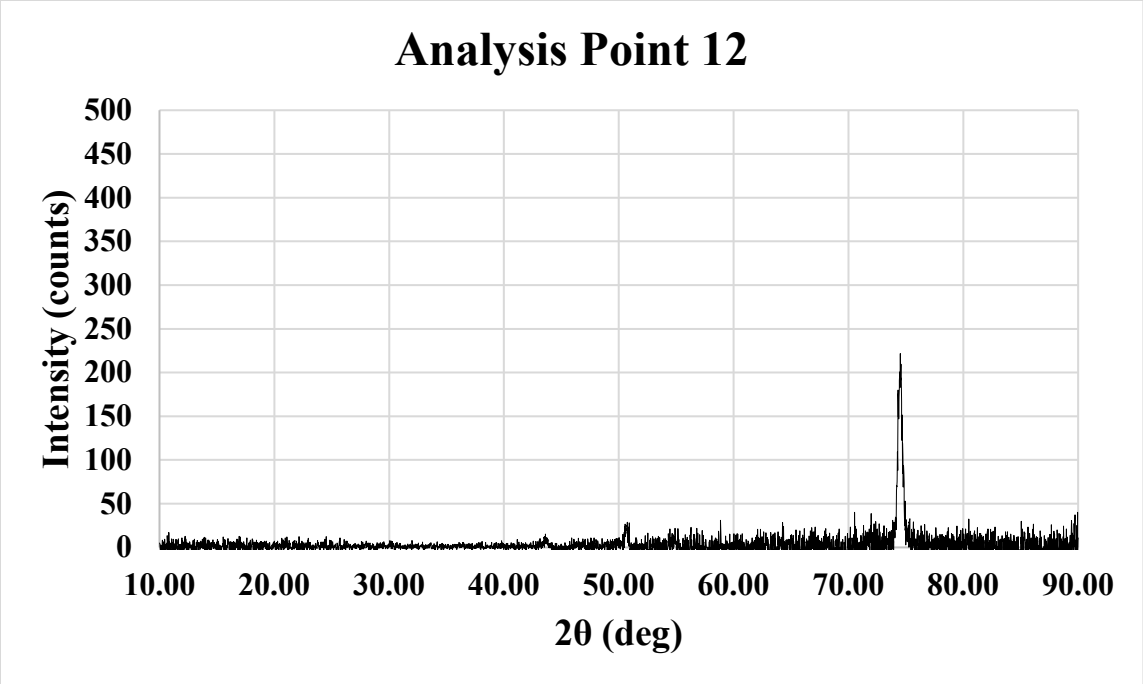

Figure 37: Raw XRD Results Analysis Point #12

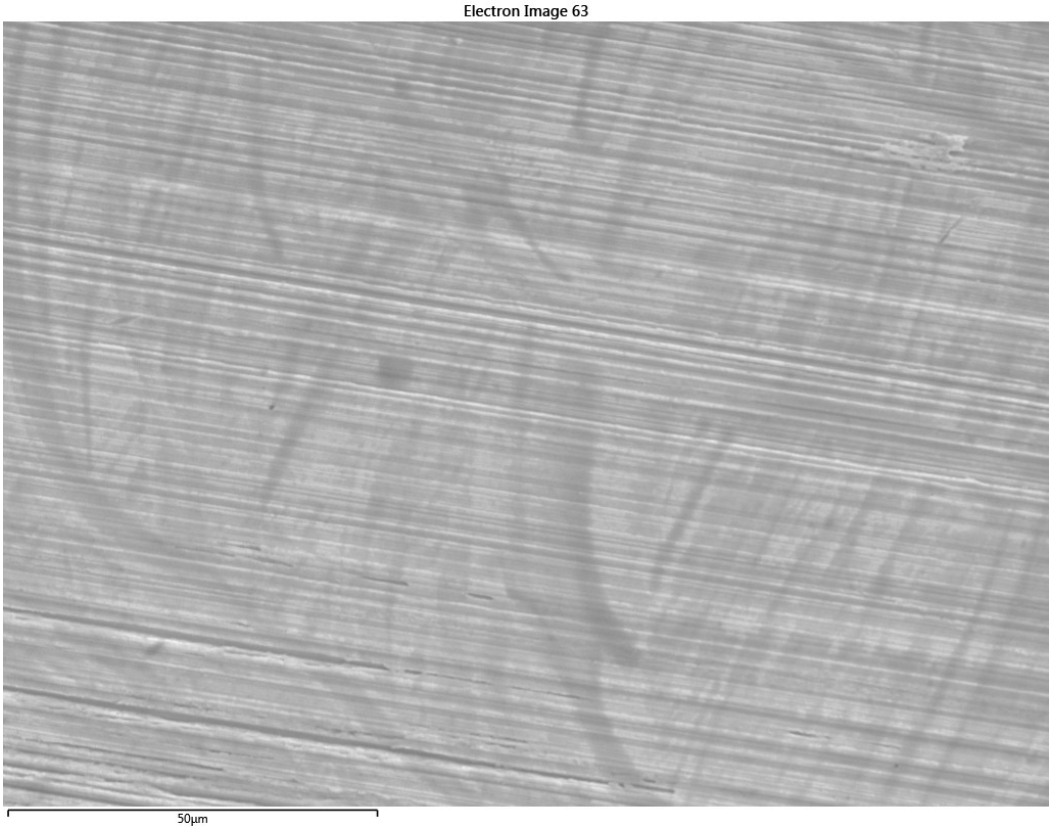

Figure 38: Analysis Points 13 SEM Micrograph of Inconel Body Center

Figure 39 details the raw EDS results from analysis point #13. The wt% values calculated from these samples are shown below in Table 15. As with other previous "center" samples the results here are similar and fall within the elemental range for pristine Inconel C-276. Overall, there does not appear to be any elemental changes at the interior from the outer wall or inner wall contamination.

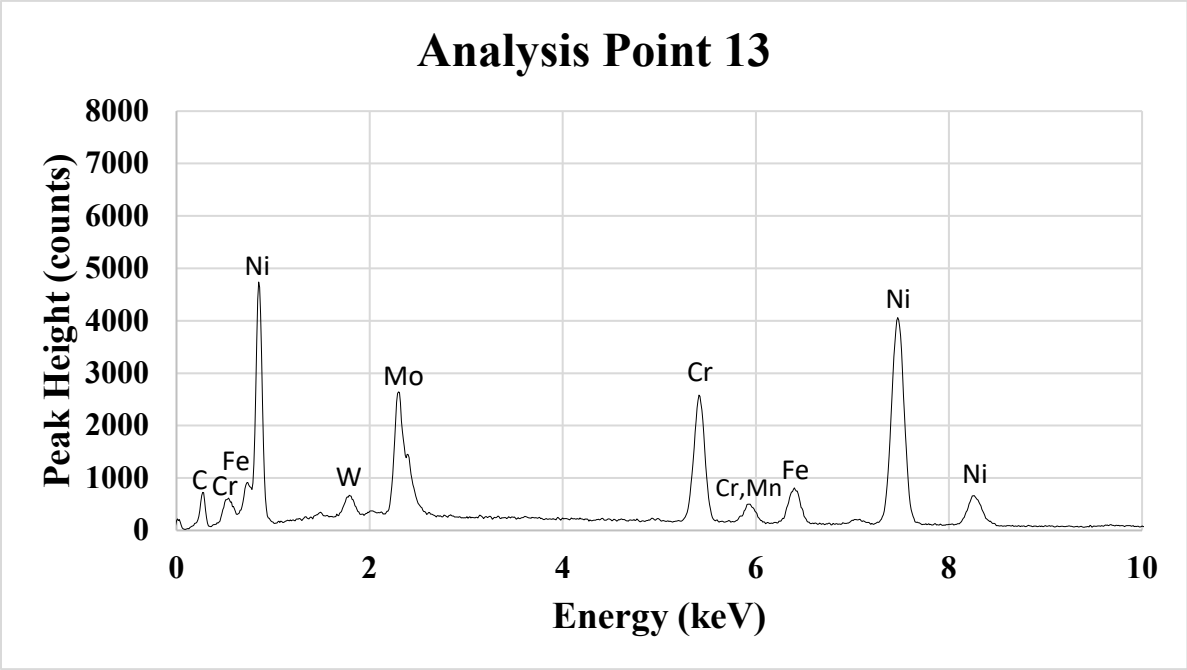

Figure 39: Raw EDS Results from Inconel Body Center at Analysis Point #13

Table 15: Analysis Point #13 for Inconel Body Element Wt%

Element Type	Point 8 Weight %
Silicon	0.00
Chromium	16.04
Manganese	0.61
Phosphorus	0.00
Nickel	56.60
Molybdenum	16.67
Iron	6.24
Cobalt	0.00
Vanadium	0.32
Tungsten	3.52

Figure 40 details the raw XRD results from analysis point #13. The peak 2θ positions are identical to the pristine Inconel sample, so no additional phases formed or significant changes in the lattice parameter occurred. The only change observed was a slight reduction in the peak ratio of the (220) and (311) peaks compared to the pristine sample, which is not significant for the purposes of this report.

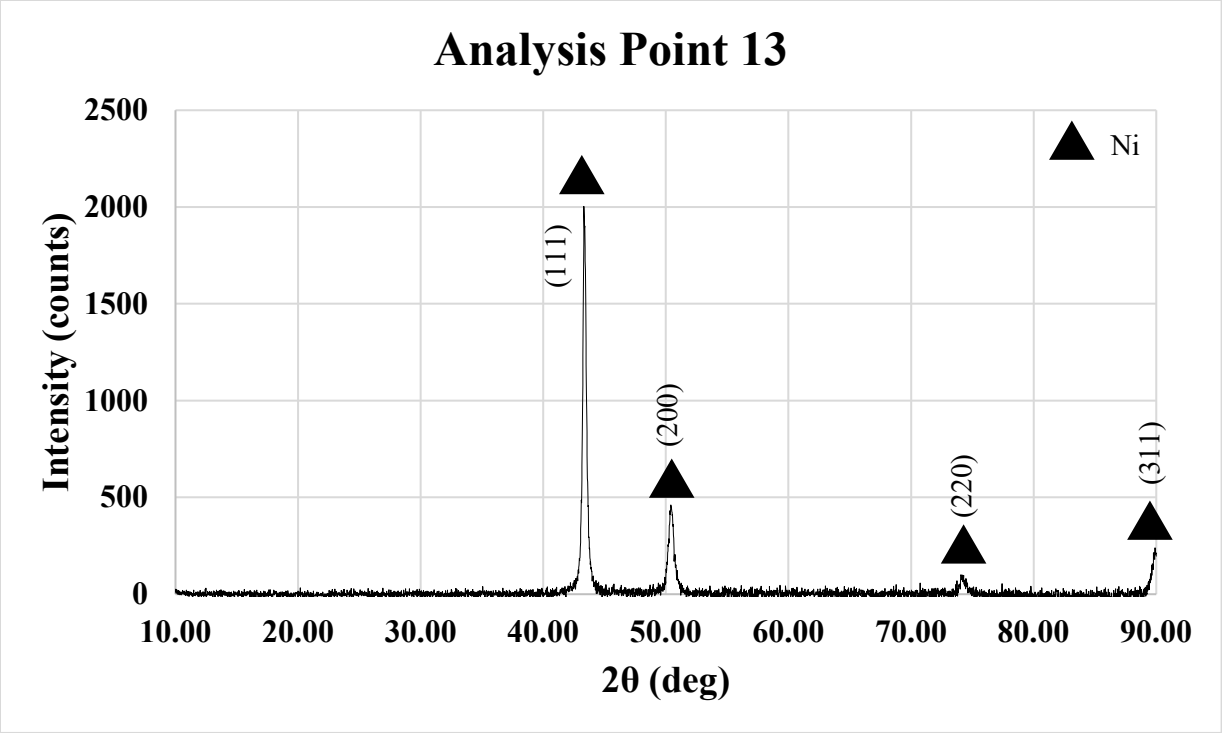

Figure 40: Raw XRD Results Analysis Point #13

Figure 41 details the SEM micrographs for the Inconel body inner wall sample at analysis point #14. The surface is rough and has deposited material, as expected.

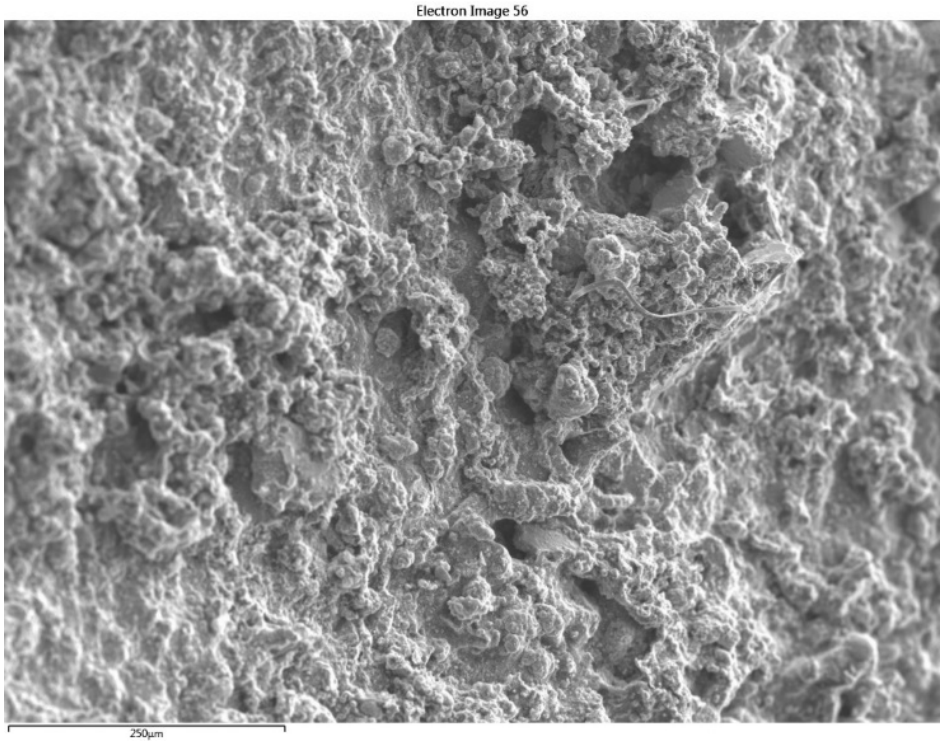

Figure 41: Analysis Points #14 SEM Micrograph of Inconel Body Inner Wall

Figure 42 details the raw EDS results from analysis point #14. The wt% values calculated from these samples are shown below in Table 16. Unsurprisingly the inner wall has elevated levels of sulfur among reduced amounts of nickel and molybdenum. There was no evidence of elevated silicon, though it could be masked underneath the surface coating.

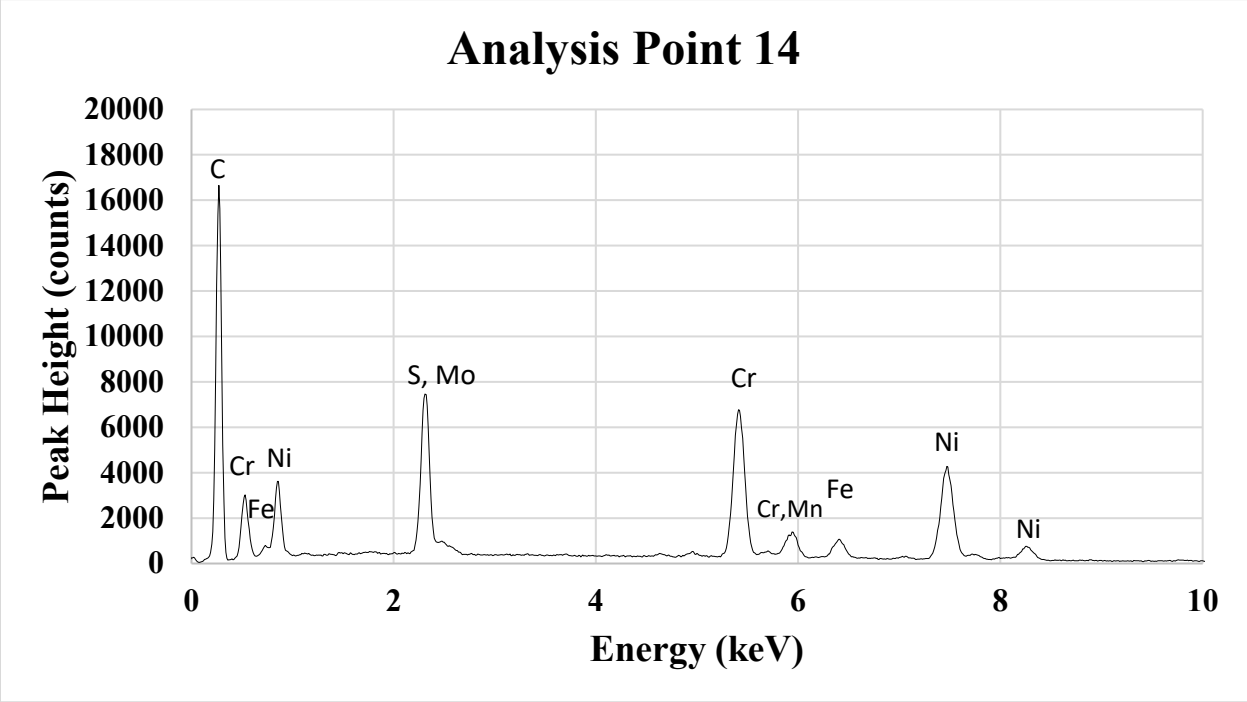

Figure 42: Raw EDS Results from Inconel Body Inner Wall at Analysis Point #14

Table 16: Analysis Point #14 for Inconel Body Element Wt%

Element Type	Point 8 Weight %
Sulfur	17.63
Chromium	32.45
Manganese	2.08
Phosphorus	0.00
Nickel	39.96
Molybdenum	5.23
Iron	4.78
Cobalt	0.00
Vanadium	1.00
Tungsten	0.00

Figure 43 details the raw XRD results from analysis point #14. The surface coating blocked the Inconel peaks somewhat as the (220) and (311) peaks are not detectable above the background, but the other two peaks are well defined. The coating appears to be amorphous since no additional peaks were present.

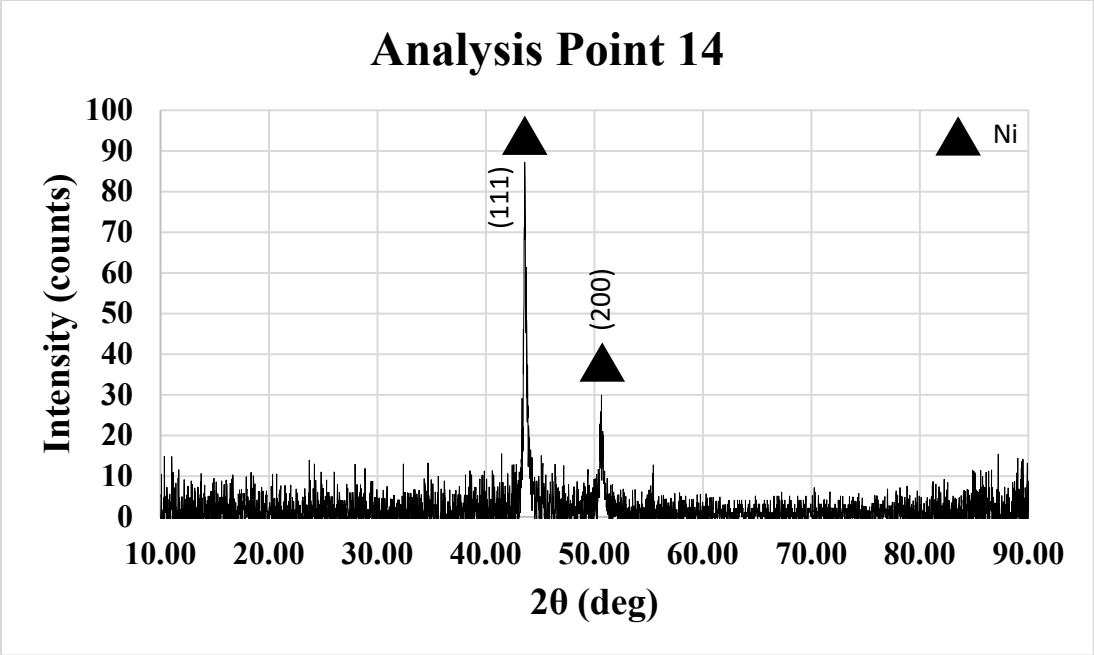

Figure 43: Raw XRD Results Analysis Point 14

3.3 High-Temperature Insulation and Heat Tape Characterization Results

This final results section details the high-temperature insulation and the heat tape used to heat the body section. Both of these potentially contain large concentrations of silicon which, if transferred, could help explain the elevated silicon found.

3.3.1 High-Temperature Insulation Results

Figure 44 details the SEM micrograph of a section from the high-temperature insulation. The insulation is composed of fibrous strands under closer inspection.

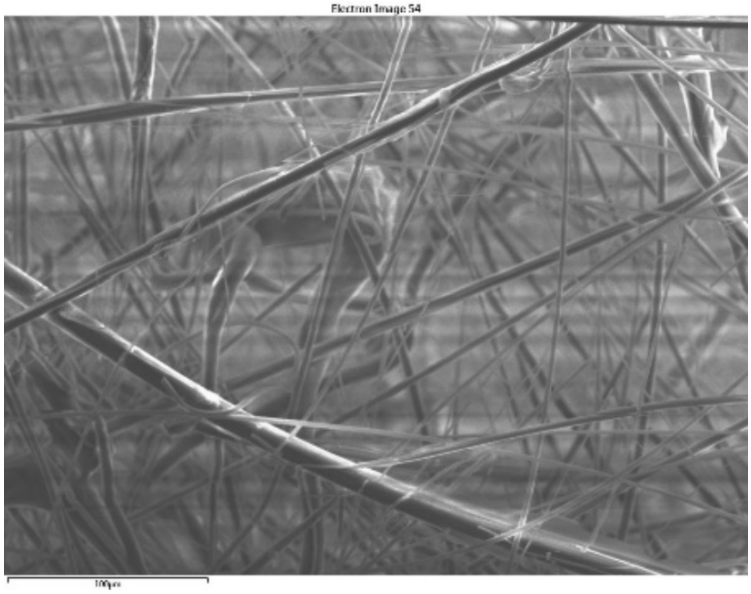

Figure 44: SEM Micrograph of High-Temperature Insulation

Figure 45 details the raw EDS results from the high-temperature insulation. The wt% values calculated from these samples are shown below in Table 17. The insulation is composed of nearly equal weight percentages of aluminum and silicon, which are both around 25 wt%. There is a large amount of silicon present in the insultation so it could be a contributor to the silicon in the Inconel.

Figure 46 details the raw XRD results from the high-temperature insulation. The insulation is highly crystalline with the aluminum producing the sharp peaks observed.

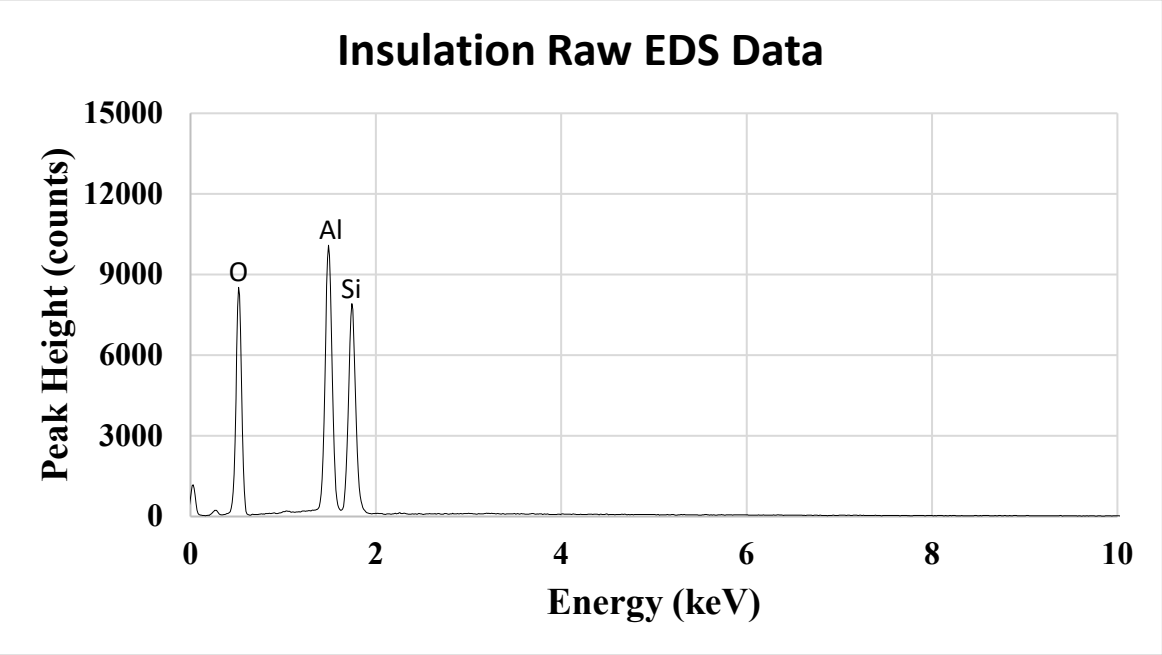

Figure 45: Raw EDS Results from High-Temperature Insulation

Table 17: High-Temperature Insulation Element Wt%

Element Type	Point 8 Weight %
Silicon	24.67
Aluminum	25.00

3.4 Heat Tape Results

Figure 47 details the SEM micrograph of a section from the heat tape used to control the temperature of the Inconel vessel. The heat tape is also made of fibrous strands, but they are held together in a more orderly fashion and look almost braided. This more ordered structure keeps the fibers together more and may prevent strands from coming off as easily.

Figure 48 details the raw EDS results from the heat tape. The wt% values calculated from these samples are shown below in Table 18. The heat tape is composed of oxygen, silicon, aluminum and magnesium. The silicon is by far the most prevalent in the heat tape as well with nearly 2/3 of the weight percentage composed of that element. This is a significant source and could be contributing to the increased silicon on the Inconel, especially since the Inconel body showed the most silicon contamination where the heat tape was being used.

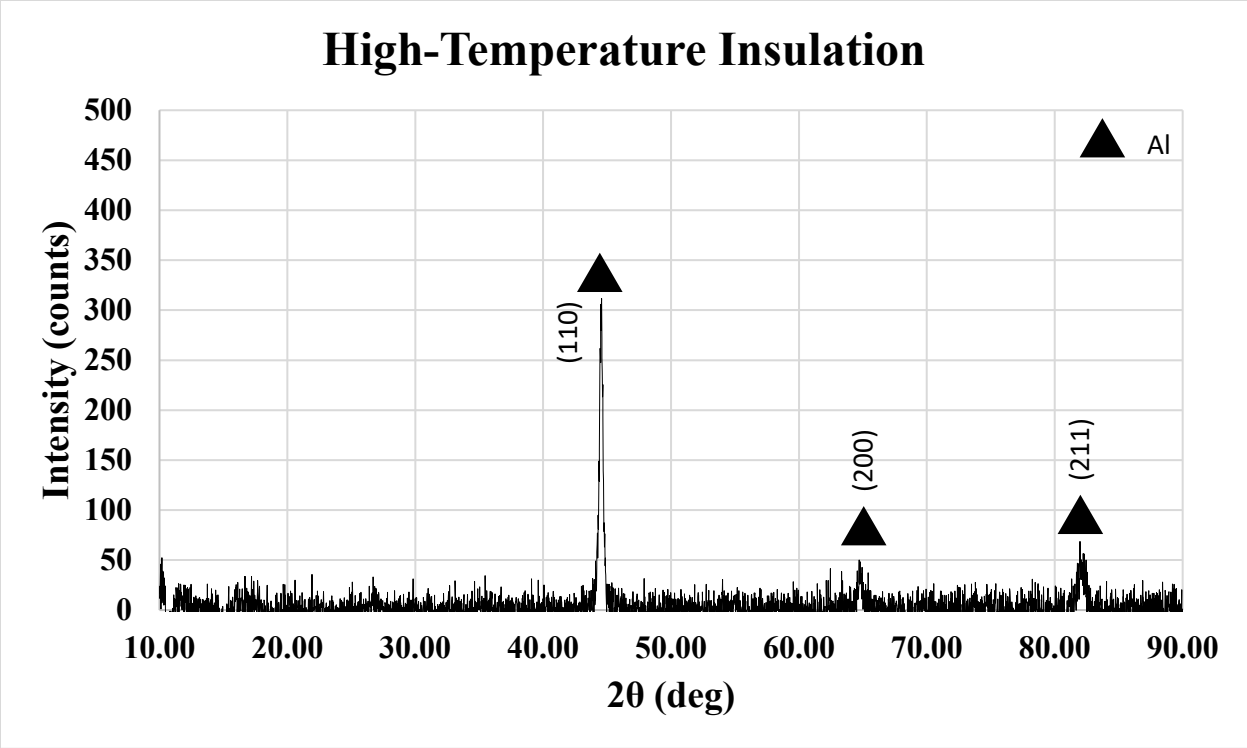

Figure 46: Raw XRD Results for High-Temperature Insulation

Figure 47: SEM Micrograph of Heat Tape

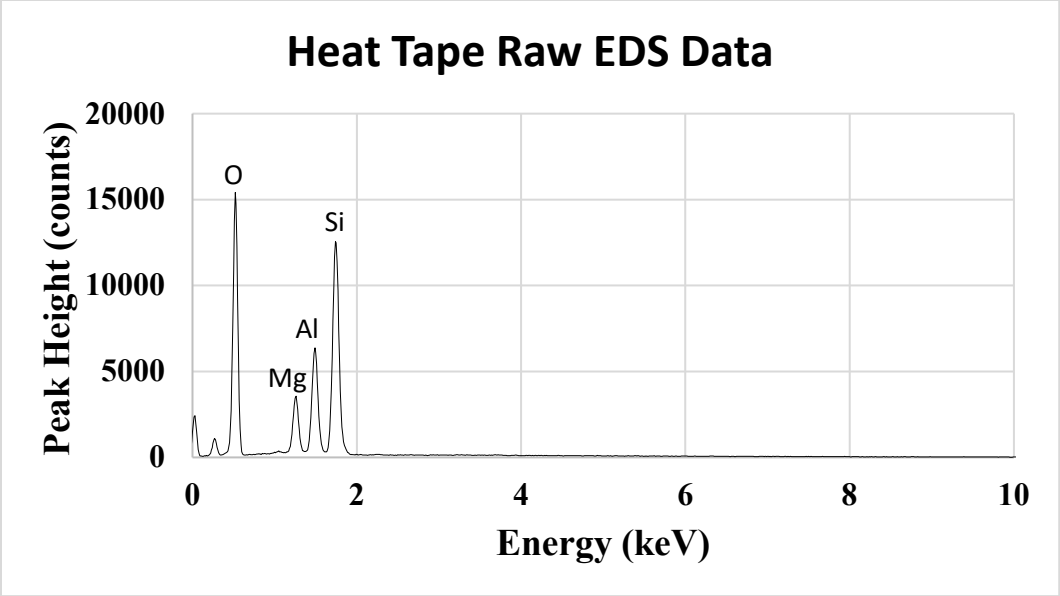

Figure 48: Raw EDS Results from Heat Tape

Table 18: Heat Tape Element Wt%

Element Type	Point 8 Weight %
Silicon	66.45
Aluminum	24.03
Magnesium	9.52

Figure 49 details the raw XRD results from the heat tape. The heat tape is extremely amorphous and does not contain any peaks. If the heat tape is structurally contaminating the Inconel it would be difficult to identify since any results would be mixed with the background information.

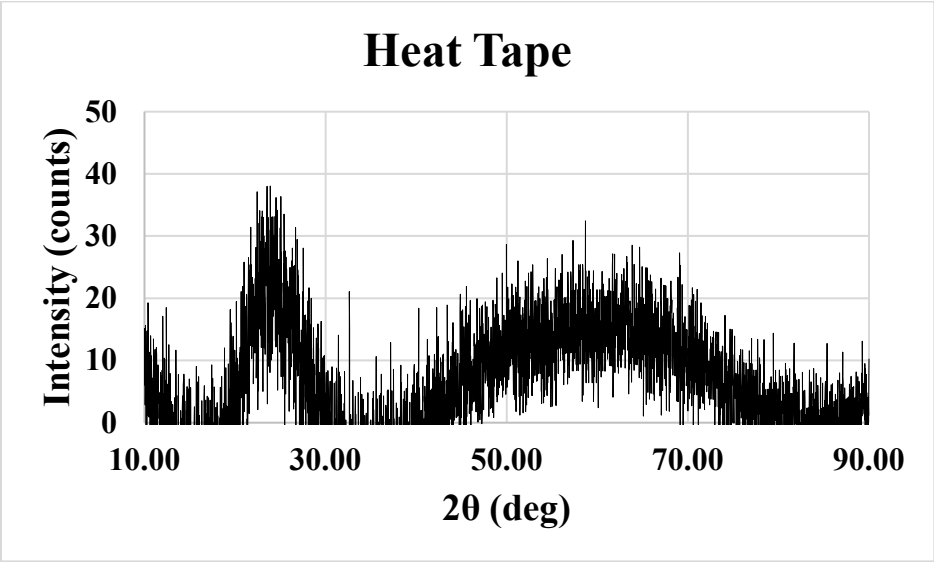

Figure 49: Raw XRD Results for Heat Tape

4.0 Conclusions

The results of these analyses illustrate interesting findings about how the two different metals used together could be degraded after being heated up to 700°C in air and high concentrations of H_2S gas.

The 316 SS fittings and tubes used were the primary failure point. This is expected since 316 SS is not as corrosion resistant as Inconel and formed a leak that started venting gas. Replacing these fittings with fittings constructed from Inconel C-276 would help mitigate this issue. However, a second failure mode was observed which may not be mitigated by changing the material of the fittings. The fitting and tube both contained a sulfur-rich deposit on the inside wall, which would have completely closed off the flow of gas. As noticed with the Inconel lid and body, the surface of Inconel does still react with H_2S so Inconel tubes and fittings may still become obstructed too.

A second point to make is that elemental diffusion did not occur throughout either the stainless steel or Inconel, which was anticipated to occur due to the elevated temperatures used. Elemental diffusion appears to be prevented since both metals formed a passivating layer on both sides (exposed to air or H_2S-rich environment). This passivating layer was not mechanically removed and thus prevented additional gas from reaching the metal surface and diffusing contaminants through the metal. This helped maintain the structural integrity of metals used.

Finally, the interior and exterior surfaces of the Inconel on the lid and body did show significant changes to their initial elemental compositions, but as mentioned, this was contained to just the surface layer. While this surface layer contamination does not appear to influence performance or safety when on the inside surface of the Inconel it does raise some concerns on the outside surface. Elevated silicon, oxygen and chromium were detected, and silicon and chromium oxides have been shown to be thermal insulators. If a thermally resistive layer was forming that could result in shortened heat tape life expectancy and potentially lower the operating temperature for the samples. This hypothesis gains more credibility as the highest concentrations of silicon, and second highest for chromium, were observed on the surface where the heat tape was used. It is unknown at this time where the elevated chromium originated from other than it diffused to the surface due to the elevated temperature. Chromium was not found in the insulation or the heat tape, so further research is required to see if diffusion could produce the elevated chromium levels. The increased silicon, on the other hand, could have come from either the insulation, the heat tape itself, or both. Additional research is needed to identify the exact source, but the results of this analysis suggest the heat tape contributed most to silicon accumulation. Thus, the heat tape is hypothesized to be the primary source of silicon contamination, based on the fact the insulation was used across all Inconel surfaces (lid and body), though the body showed exponentially more contamination. The heat tape was also in closer proximity to the Inconel and would have transferred silicon more readily. The thermal conductivity of the Inconel body surface needs to be performed to be conclusive. Even if the heat tape is primary cause, it may be difficult to find an alternative as resistive heating elements are many times constructed using silicates.

In conclusion, material analysis of the 316 SS and Inconel showed the 316 SS inlet tube and fittings were susceptible to being oxidized and their flow closed from sulfur deposits. Analysis also showed that the use of silicon-containing insulation and heat tape may be decreasing the life expectancy of the heat tape through silicon being deposited on the Inconel surface. Further research is required to determine if this conclusion holds, but potentially replacing the heat tape with another heating approach such as heated air or induction may need to be explored.

References

[1] S. S. Company, "Sandmeyer Steel Company," 2022. [Online]. Available: https://www.sandmeyersteel.com/316-316L.html#ChemicalAnalysis. [Accessed 2022].

[2] A. Materials, "Azo Materials," 2022. [Online]. Available: https://www.azom.com/article.aspx?ArticleID=2868. [Accessed 2022].

[3] P. Chattopadhyay, A. Samanta, W. Lojkowski, H.-J. Fecht and I. Manna, "Microstructure/Phase Evolution in Mechanical Alloying/Milling of Stainless Steel and Aluminum Powder Blends," *Metall. Mater. Trans. A,* vol. 38A, pp. 2298-2307, 2007.

[4] S. S. Company, "Sandmeyer Steel Company," 2022. [Online]. Available: https://www.sandmeyersteel.com/C276.html. [Accessed 2022].

[5] MatWeb, "MatWeb Material Property Data," 2022. [Online]. Available: https://matweb.com/search/datasheet.aspx?matguid=24441921ff1d43cbbc473ecc672d1b6b&ckck=1. [Accessed 2022].